Montanuniversität Leoben

DIPLOMA THESIS

Oxidation Behaviour of a Novel Nanolamellar $Ti_{0.05}Al_{0.95}N$ Coating

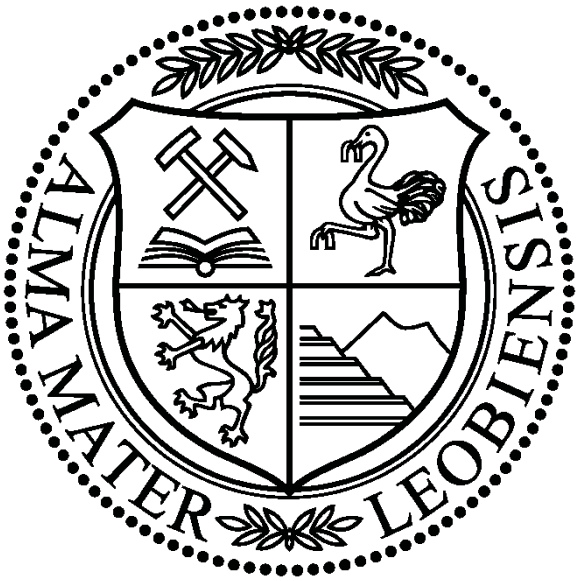

by

Juraj Todt

The work presented in this thesis was conducted at the Department of Materials Physics of the University of Leoben and at the Erich Schmid Institute of the Austrian Academy of Sciences.

Leoben, September 2013

AFFIDAVIT

I declare in lieu of oath, that I wrote this thesis and performed the associated research myself using only literature cited in this volume.

EIDESTATTLICHE ERKLÄRUNG

Ich erkläre an Eides statt, dass ich diese Arbeit selbstständig verfasst, andere als die angegebenen Quellen und Hilfsmittel nicht benutzt und mich auch sonst keiner unerlaubten Hilfsmittel bedient habe.

September 2013

Acknowledgements

I would like to thank my parents Mag. Jürgen Todt and Dr. Alena Todtova who have always supported me in any way imaginable and to whom I will be eternally grateful. My sister Kristina Todtova was always there for me to talk things through and I am very thankful for her company past, present and future.

As well, I would like to thank my friends for the great times that I had with them and especially for their committed discussions and distractions from day-to-day life when I needed them.

I feel a very special gratefulness towards my advisor Dr. Jozef Keckes whose nature made it a pleasure to be working with him and who besides to always being available for professional support, I am also happy to call a friend.

The same is true for Dipl.-Ing. Josef Kreith, Dr. Matthias Bartosik, Dipl.-Ing. Marlene Kapp and Dr. Christoph Kirchlechner who are or were the colleagues in my office and also the many others that work elsewhere at the institute. They have always been a great and unlimited source for insightful and lively conversations.

My gratitude is also directed towards Dr. Thomas Schöberl who supervised nanoindentation measurements, RNDr. Igor Matʹko who was responsible for TEM and HRTEM images, Gabriele Moser who expertly prepared the samples for synchrotron measurements and Dipl.-Ing. Angelika Riedl and Bernhard Sartory who managed SEM imaging and FIB milling.

I would also like to thank Dr. Reinhard Pitonak from Böherit GmbH & Co. KG in Kapfenberg who manufactured the investigated coatings and provided us with samples. Finally I want to express my gratitude towards the beamline staff at the ID13 beamline of the ESRF in Grenoble without whom the synchrotron measurements would not have been possible.

Abstract

Protective hard coatings based on a novel nanostructured $Ti_{0.05}Al_{0.95}N$ layer prepared by low pressure chemical vapour deposition were characterized with respect to their oxidation behaviour at 700 – 1150 °C in terms of phase evolution, microstructural changes, residual stress evolution and hardness. A comparison with other coatings prepared by two different physical vapour deposition methods that are in common use comprehensively demonstrated the superior oxidation resistance of the novel coating. The formation of the protective α-Al_2O_3 (corundum) surface layer that is held responsible for this quality could be documented with laboratory and synchrotron X-ray diffraction techniques as well as electron microscopy. Employing high resolution transmission electron microscopy a new self-organized nanoscale lamellar microstructure in the $Ti_{0.05}Al_{0.95}N$ layer was discovered. Depth-resolved hardness measurements on a wedge cut into the coating by focused ion beam milling were carried out by nanoindentation and revealed an unexpectedly high hardness of the highly Al-rich layer that can be explained by the aforementioned microstructure. Finally, synchrotron X-ray diffraction showed no particularly strong preferred orientation in the coating and depth-resolved residual stress profile evaluation evidenced a complex graded compressive stress state that partly relaxes due to phase decomposition after high temperature oxidation.

Kurzfassung

Verschleißschutz-Beschichtungen basierend auf einer neuartigen nanostrukturierten über ein "low pressure chemical vapour deposition"-Verfahren hergestellten $Ti_{0.05}Al_{0.95}N$ Schicht, wurden bezüglich ihrer Oxidationseigenschaften im Temperaturbereich von 700 °C – 1150 °C in Hinblick auf Phasenzusammensetzung, Gefügeänderungen, Eigenspannungsentwicklung und Härte untersucht. Ein Vergleich mit anderen Beschichtungen, die mittels zweier unterschiedlicher "physical vapour deposition"-Verfahren abgeschieden wurden und weit verbreitet Anwendung finden, demonstrierte anschaulich den überlegenen Oxidationswiderstand der neuen Beschichtung. Die Bildung einer schützenden α-Al_2O_3 (Korund) Deckschicht, die für diese Eigenschaft verantwortlich gemacht wird, konnte mit Labor- und Synchrotron-Röntgendiffraktion, als auch mit Elektronenmikroskopie-Methoden dokumentiert werden. Durch den Einsatz hochauflösender Transmissions-Elektronenmikroskopie wurde eine neue lamellare Phase in der $Ti_{0.05}Al_{0.95}N$ Schicht mit charakteristischen Längen im Nanometer-Bereich entdeckt. Tiefenaufgelöste Härtemessungen mittels Nanoindentation auf einem flachen Keil, der mit einem fokussierten Ionenstrahl in die Beschichtung geschnitten wurde, offenbarten eine unerwartet hohe Härte der hoch Al-haltigen Schicht, welche durch das zuvor erwähnte nano-lamellare Gefüge erklärt werden kann. Schließlich zeigte Synchrotron-Röntgendiffraktion keine besonders ausgeprägten Vorzugsorientierungen in der Beschichtung und tiefenaufgelöste Eigenspannungsmessungen belegten einen komplexen tiefenabhängigen Druckspannungszustand, welcher durch Phasenzersetzung während der Oxidation bei hohen Temperaturen teilweise relaxiert.

Table of Contents

1. Introduction and Motivation

Protective hard nitride coatings have been widely used to improve the performance of devices and components experiencing high mechanical and thermal loads, such as cutting tools and casting moulds. This is due to their high wear resistance which is based on their thermal stability, high hardness and low coefficient of friction. Tool lifetime can thus be increased considerably and is mainly limited by coating oxidation occurring at high temperatures in ambient air atmosphere. To counter oxidation and to expand the range of use, cubic $Ti_{1-x}Al_xN$ coatings were developed and have been available for about 25 years [1, 2].

$Ti_{1-x}Al_xN$ coatings are mainly produced by physical vapour deposition (PVD), where the constituent elements of the coating are vaporized by physical means into a stream of atoms which is then condensed onto the substrate (the object that should be coated). Another possibility to grow such coatings is chemical vapour deposition (CVD), where the precursor materials are supplied in form of gaseous chemical compounds that contain the constituent elements which then decompose near the substrate surface and subsequently condense onto it. PVD is easier to control than CVD and it lacks the dangerous precursor gases of the latter as well as the necessity for high deposition temperatures, but growth rates and film composition homogeneity are still better using CVD processes [3, p.145ff].

The introduction of Al into TiN brings about the formation of new phases, an increase in hardness and most notably an increase in oxidation resistance [2, 4]. It has been observed that a higher Al content is particularly beneficial regarding the resistance to oxidation. This is attributed to the formation of a protective aluminium oxide top layer that is very dense and hinders further oxidation. Therefore it seems desirable to manufacture $Ti_{1-x}Al_xN$ coatings with a very high Al content. Some problems with this approach have been encountered, namely when the solubility limit (typically $x = ⅔$) of Al in $Ti_{1-x}Al_xN$ is exceeded in PVD sputtered coatings which leads to a softer and electrically insulating hexagonal AlN phase being co-deposited [5, 6]. Moreover, upon annealing of cubic $Ti_{1-x}Al_xN$ coatings with a sufficient Al content spinodal decomposition occurs that can lead to hardness increase or decrease and coating decohesion [7]. For this reason, coatings with a limited Al content that only contain a hard cubic TiAlN mixed phase have been favoured until recently [4].

Using a novel low-pressure chemical vapour deposition (LPCVD) process in order to lower deposition temperatures and hence change overall deposition conditions it was recently possible to manufacture $Ti_{1-x}Al_xN$ coatings with x up to 0.9 and with only the desired cubic (fcc) TiAlN mixed phase present in the as-deposited state [8]. Furthermore it could be shown that the cubic phase was stable up to temperatures exceeding 1100 °C during annealing in vacuum conditions. The study of the behaviour of such $Ti_{1-x}Al_xN$ coatings during annealing in ambient air and with even higher Al contents promises to bring interesting results and is the main focus of this diploma thesis.

For this purpose, a coating with an Al content of $x = 0.95$ was manufactured by the above-mentioned LPCVD process on WC-Co cemented carbide cutting inserts. The $Ti_{1-x}Al_xN$ layer is part of a sophisticated multi-layer coating system that is designed to optimize the overall

adherence and hardness of the coating. Samples were annealed in ambient air at temperatures ranging from 700 °C to 1150 °C and a phase analysis was carried out for each of the samples in order to monitor the formation of the protective aluminium oxide top layer and the evolution of the phase composition inside the $Ti_{1-x}Al_xN$ layer.

To obtain information on the morphology of these phases, images of a coating cross-section were recorded in a high resolution transmission electron microscope (HRTEM). There, it was also possible to identify phases using selected area diffraction (SAD) and energy dispersive X-ray spectroscopy (EDX) [9]. Further information on phase composition and morphology was obtained by X-ray diffraction (XRD) with a laboratory instrument in surface-sensitive grazing-incidence mode and with a scanning electron microscope (SEM) that was also capable of EDX [10].

With regard to mechanical properties, hardness was measured by nanoindentation on a wedge cut into the coating with a focused ion beam (FIB) [11]. Indents on the wedge can be used to obtain depth-resolved information on hardness, because their lateral position corresponds to a specific depth inside the coating.

Finally, also depth-resolved residual stresses and crystallographic texture were characterized by scanning a cross-sectional lamella cut out of a sample with a very narrow X-ray beam while recording powder diffraction patterns. When elastic strain is present in the irradiated volume, then the Debye-Scherrer rings that form the diffraction pattern of polycrystalline thin films are distorted elliptically. The amount of distortion is proportional to the amount of strain, which can be calculated thus. The X-ray beam has to have a diameter well below the coating thickness, typically in the nanometre range and therefore this method is called *cross-sectional X-ray nanodiffraction* and is currently available only at European synchrotron sources providing high brilliance radiation [12-14].

Residual stresses in coatings are formed during film growth with the major mechanisms being thermal expansion coefficient mismatch and in case of PVD crystallographic growth defects due to particle impingement that governs the growth kinetics of these processes [3, p.742ff; 15, p.60ff]. However it is also common to introduce residual stresses deliberately after deposition in order to alter the mechanical performance of coatings through surface treatments like shot-peening which is also frequently used for surface-hardening of bulk metallic components. Hardness, and more importantly coating and tool lifetime can thus be influenced in a major way. Especially compressive residual stresses are regarded as beneficial, as they counteract tensile stress states which in their turn facilitate crack initiation and growth that govern material fatigue and wear.

2. Experimental Methods

2.1. X-ray Diffraction (XRD)

X-rays are scattered by the electron clouds of atoms and therefore can be used as a probe for the corresponding length scale. Both characteristic dimensions (wavelength λ and atom diameter d) are in the order of 1 Å or 10^{-10} m. Electromagnetic waves that are scattered from regularly arranged scattering sites, such as an atomic lattice, interact with each other by wave superposition which results in constructive or destructive interference. The Bragg condition describes the circumstances of constructive interference of X-rays on an atomic lattice as it is encountered inside crystalline solids like metals and ceramics but also more complex materials. As an equation it is given by

$$n\lambda = 2d \sin\theta \tag{2.1}$$

where n is an integer value (the diffraction order) and θ is half the diffraction angle 2θ, which is the angle between the primary beam and the diffracted beam [16, p.82]. In this case d is the spacing of crystallographic lattice planes. (Fig. 2.1)

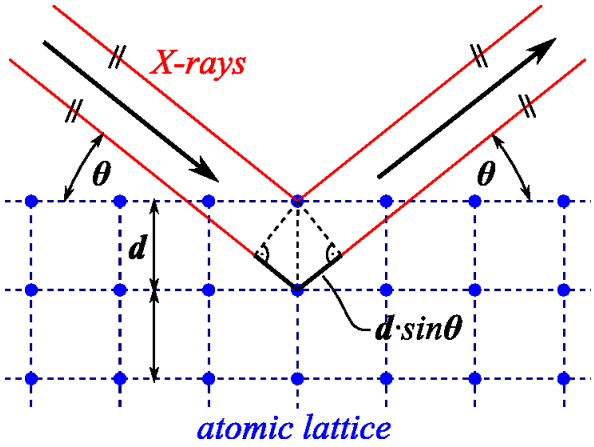

Fig. 2.1: Bragg condition shown schematically on a 2D array of dots that represent an atomic lattice.

In addition to fulfilling the Bragg condition also the so-called structure factor F_{hkl}, which takes into account the crystal structure (particularly the unit cell), needs to yield a value greater than zero for a hkl combination of Miller indices. It can be calculated as follows [16, p.74]:

$$F_{hkl} = \sum_n f_n e^{i\vec{H}_{hkl}\vec{r}_n} \tag{2.2}$$

$\vec{H}_{hkl}$ is the reciprocal space vector of the lattice planes denoted by the index hkl [16, p.52ff]. $\vec{r}_n$ is the position vector of the n^{th} atom within the unit cell and f_n is the form factor of the corresponding atom. By solving eq. 2.2 a rule for each crystal structure can be derived as to for which combination of *h, k* and *l* a constructive interference can be observed. For instance in body centred cubic (bcc) crystal structures the sum ($h + k + l$) needs to be even so that F_{hkl} is not zero.

Untextured polycrystalline materials and crystalline powders consist of randomly oriented crystallites and hence diffraction cones with a specific opening angle 4θ are observed in transmission geometry when many grains are irradiated with a macroscopic X-ray beam. Textured polycrystalline materials differ from this in that their crystallites have a preferred orientation and are no longer randomly aligned with respect to each other.

By moving an X-ray source and/or an X-ray detector so as to scan the diffraction angle 2θ and by measuring the X-ray beam intensity along the way, a so-called *powder diffraction pattern* is recorded [16, p.141]. For this purpose the source, sample and detector are fixed to a *goniometer* that can provide the necessary movements and measure precisely the relative angles between the corresponding parts. The setup including a suitable goniometer with an X-ray source and a detector is called a *diffractometer*. These instruments often offer additional rotational and translational axes for more complex measurements that require control over the orientation and position of the sample. A very common setup is a 4-circle diffractometer, because it allows for texture and residual stress analysis and other useful measurements [16, p.142]. (Fig. 2.2)

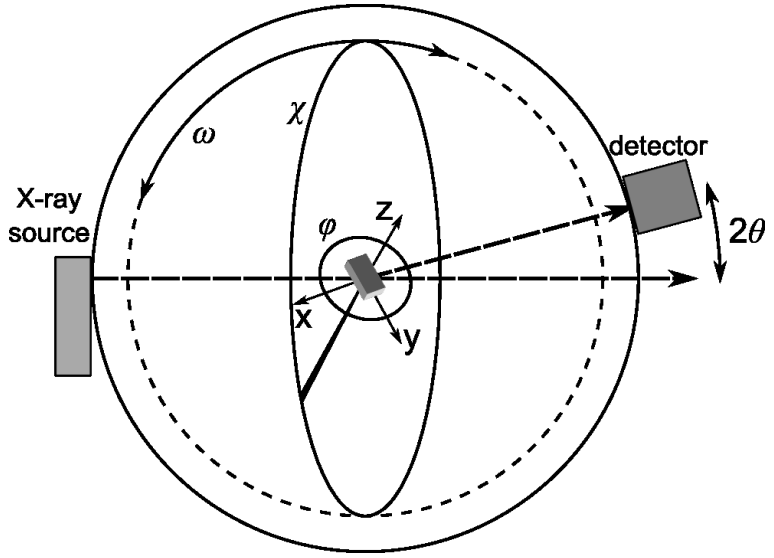

Fig. 2.2: Axes and angles of a 4-circle diffractometer. x, y, z and φ are motions made by a sample stage which itself can be tilted sideways around χ and in the 2θ rotation plane by a "2θ offset angle" ω.

2.1.1. Phase Analysis

Most crystalline materials can be identified by comparing a measured powder diffraction pattern with a pattern from a database [16, p.224f]. Because this method is sensitive to the crystal structure, different phases of the same chemical composition (*polytypes*) can be distinguished.

Some influences and limitations have to be considered when a phase analysis is carried out by powder diffraction:

- Because the method relies on diffraction, only crystalline phases can be identified. Amorphous phases contribute to the diffraction pattern only in the way of very broad

peaks with a very low intensity that blend into the background noise level and have their origin in the short-range order of amorphous materials.

- The integrated area of a diffraction peak is proportional to the volume fraction of the corresponding phase within the irradiated volume. This means that there is a lower limit for the peak intensity that determines phase detectability and is given by the achievable signal to noise ratio. Because primary beam intensities are limited in laboratory instruments the most significant contribution to this aspect is the background noise level [16, p.234ff].
- The penetration depth and thereby also the irradiated volume is determined by the X-ray beam energy, the sample material absorption coefficients and geometrically, mainly by the primary beam incidence angle. In a laboratory diffractometer it is not practicable to change the beam energy frequently, so the penetration depth is controlled by the incidence angle. From a low angle follows a shallow penetration depth and thus very surface-sensitive measurements are possible. This measurement mode is called *grazing incidence* [16, p.71,186ff].

2.1.2. Residual Stress Characterization

When a powder diffraction pattern is recorded in laboratory conditions the diffraction vector $\vec{Q}$, which is the difference vector between the incidence wave vector $\vec{k}_0$ and the diffracted wave vector $\vec{k}_1$ and is perpendicular to the diffracting lattice planes, usually remains perpendicular to the sample surface during the measurement [16, p.83]. (Fig. 2.3) This is done by putting the sample with its surface parallel to the direct beam direction and moving the X-ray source by θ and the detector by θ in the opposite direction or by moving the sample by θ and the detector by 2θ in the same direction [16, p.141].

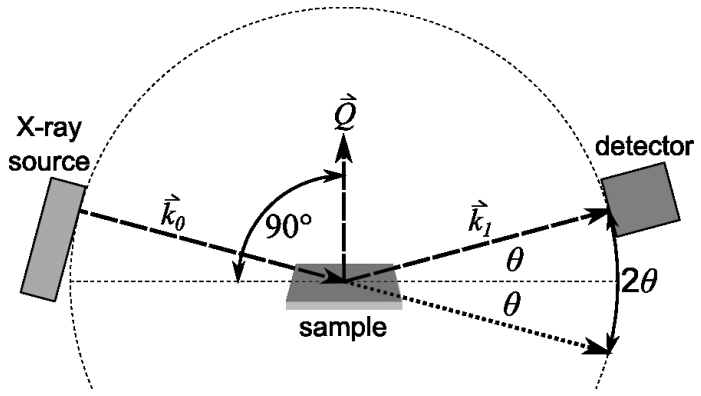

Fig. 2.3: In a conventional $\theta/2\theta$ scan the diffraction vector $\vec{Q}$ always remains perpendicular to the sample surface.

For a stress measurement the χ axis (Fig. 2.2) is used to tilt the sample sideways while $\vec{Q}$ stays fixed, which is equivalent to tilting $\vec{Q}$ with respect to the sample. The angle between the sample surface normal vector and the diffraction vector is commonly called ψ [16, p.352].

From the 2θ position of a peak the spacing d of the corresponding lattice planes can be calculated. (See eq. 2.1) Under elastic strain along $\vec{Q}$, the lattice spacing changes according to

$$\varepsilon(hkl) = \frac{d(hkl) - d_0(hkl)}{d_0(hkl)} \tag{2.3}$$

where $d_0(hkl)$ denotes the unstrained lattice spacing and $\varepsilon(hkl)$ is the elastic strain of the lattice planes perpendicular to $\vec{Q}$ [16, p.333]. By tilting $\vec{Q}$ through ψ the X-ray elastic strain $\varepsilon(hkl)$ can be accessed at different orientations of $\vec{Q}$ with respect to the sample surface normal ranging from perpendicular to parallel to the sample surface. In a quasi-isotropic biaxially strained sample $d_{\varphi,\psi}(hkl)$, measured at distinct sample orientations given by φ and ψ, has a linear dependence on $\sin^2\psi$ and can be used to calculate the stress in the in-plane direction of the sample as follows [17, p.122f]:

$$\frac{\partial d_{\varphi,\psi}(hkl)}{\partial \sin^2\psi} = \frac{S_2(hkl)}{2}\sigma_{\parallel\varphi} d_0(hkl) \tag{2.4}$$

In laboratory XRD the employed radiation penetrates only the topmost few microns of a sample, so the probed volume is always under biaxial or uniaxial strain. For equibiaxially strained samples $d_\psi(hkl)$ and the in-plane stress $\sigma_\parallel$ are independent of φ. $\frac{S_2(hkl)}{2}$ is the appropriate X-ray elastic constant of the measured sample material and can be expressed through the material-specific and hkl-dependent Poisson's ratio $\upsilon(hkl)$ and Young's modulus $E(hkl)$ as [16, p.332]

$$\frac{S_2(hkl)}{2} = \frac{1+\upsilon(hkl)}{E(hkl)} \tag{2.5}$$

Residual stresses are calculated by solving eq. 2.4 for $\sigma_\parallel$ and they are averages over the irradiated volume [16, p.327].

2.2. Synchrotron Nanodiffraction

2.2.1. X-ray Generation at Synchrotrons

Originally conceived as particle accelerators for high-energy physics experiments, synchrotrons offer unique possibilities for light generation. Unlike linear accelerators, synchrotrons make use of storage rings that require acceleration of particles towards the centre of the ring to bend their flight path into a ring shape. During this acceleration, electromagnetic radiation is emitted tangentially from the flight path of the charged particles.

Modern synchrotron sources make use of specialized magnetic devices that *undulate* and *wiggle* charged particles flying at relativistic speeds to take advantage of interference effects in order to generate radiation with tuneable properties [16, p.93ff]. In combination with further optical devices it is thus possible to produce X-ray beams with nearly arbitrary spectral distribution and exceptionally high brilliance, i.e. very high photon flux densities and

very low beam divergence. The photon fluxes achievable at a synchrotron light source are many orders of magnitude higher than those available under laboratory conditions.

2.2.2. Cross-sectional X-ray Nanodiffraction

When a crystalline sample is thin enough to be transparent for X-rays of a specific energy, a diffraction pattern can be recorded by a two-dimensional (2D) detector behind the sample. In the case of polycrystalline or powdered samples the diffraction patterns take the form of so-called *Debye-Scherrer* rings that represent the intersection of diffraction cones with the detector plane. These diffraction patterns contain information on the phases present in the illuminated volume, their preferred crystallographic orientation, crystallite size and their elastic strain. (Fig. 2.4)

By making the irradiated volume very small, i.e. lowering the beam diameter, highly localized probing of a sample becomes possible. Because thin films used as hard protective coatings in industry have a typical thickness of a few microns, it is necessary to focus the beam diameter down to a fraction of this length. This can be done for instance by special elliptically shaped focusing mirrors, so-called *Kirkpatrick-Baez mirrors*, which need to have extremely low surface roughness and geometry deviation [18-20].

A synchrotron X-ray beam focused down to a few 10 or 100 nm can then be used to scan a cross-section of a thin specimen and subsequently to correlate data acquired from a diffraction pattern with the respective position on the sample cross-section [12, 13].

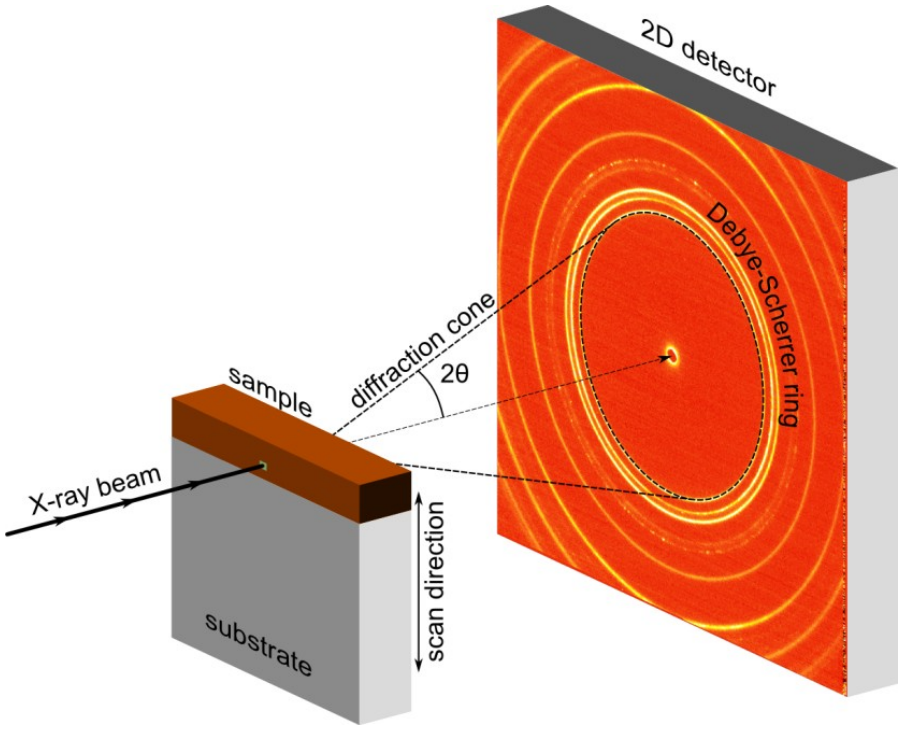

Fig. 2.4: Cross-sectional X-ray nanodiffraction on a thinned coating-on-substrate sample. In order to obtain depth-dependent thin film properties, the sample cross-section is scanned with a very narrow X-ray beam.

2.2.3. Phase Analysis

Phase analysis of 2D powder diffraction patterns essentially works in the same way as with laboratory $\theta/2\theta$ powder diffraction patterns. However an intermediary step is necessary to extract $\theta/2\theta$ data from the recorded 2D images. This is done by integrating them azimuthally [21]. (Fig. 2.5) The resulting one-dimensional intensity data represent an average over all directions covered by the diffraction ring.

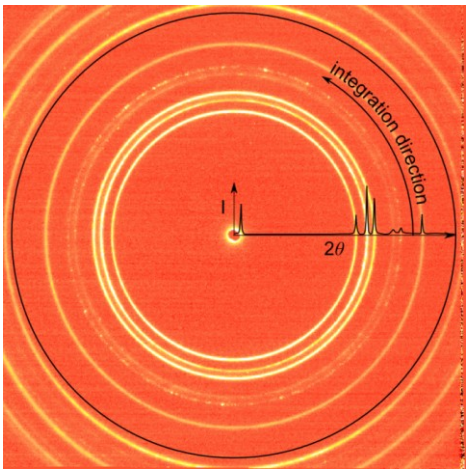

Fig. 2.5: Azimuthal integration of Debye-Scherrer rings in order to extract θ/2θ data.

2.2.4. Crystallographic Texture Analysis

A preferred orientation of crystallites can be extracted from 2D powder diffraction patterns by considering the azimuthal changes of intensity along a Debye-Scherrer ring. Commonly texture can be expressed by a pole figure which is a stereographic projection of diffraction peak intensities for distinct orientations of the diffraction vector in the sample coordinate system [16, p.381f]. (Fig. 2.6)

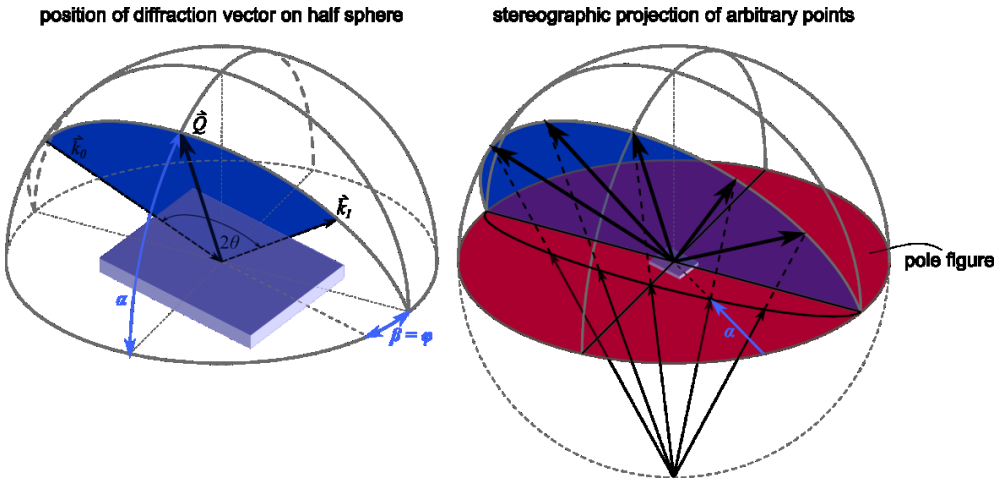

Fig. 2.6: A pole figure is the stereographical projection of diffraction intensities that are plotted where a respective diffraction vector intersects with one hemisphere of orientation space.

In laboratory instruments it is hence necessary to tilt and rotate the measured sample around the diffractometer φ and χ axes (Fig. 2.2) in order to move the diffraction vector through orientation space and thus record orientation-dependent diffraction intensities [16, p.390ff].

Polycrystalline thin films usually exhibit a fibre texture which means that crystallites are oriented with one crystallographic direction parallel to a certain sample direction. Usually, in fibre-textured thin films the fibre axis is oriented perpendicular to the substrate surface which means that a certain family of lattice planes is oriented parallel to the surface. This can be seen as rings in a pole figure [16, p.384].

The 2D diffraction pattern gathered by transmission XRD represents a segmental cut through the sphere of diffraction vector orientation space and can be seen as a curved line inside the corresponding pole figure. (Fig. 2.7) By considering the azimuthal intensity profile of a Debye-Scherrer ring, the respective pole figure and thereby also the respective fibre texture can be deduced.

The azimuthal angle δ in the diffraction pattern can be correlated to the polar angle α in the pole figure and by comparing intensity distributions with known pole figures a conclusion concerning the fibre texture of the sample is drawn then. In case $\delta = 0°$ and $\alpha = 0°$ both lie in the horizontal direction, the relationship between α and δ is given by

$$\sin^2 \alpha = \cos^2 \theta \sin^2 \delta \tag{2.6}$$

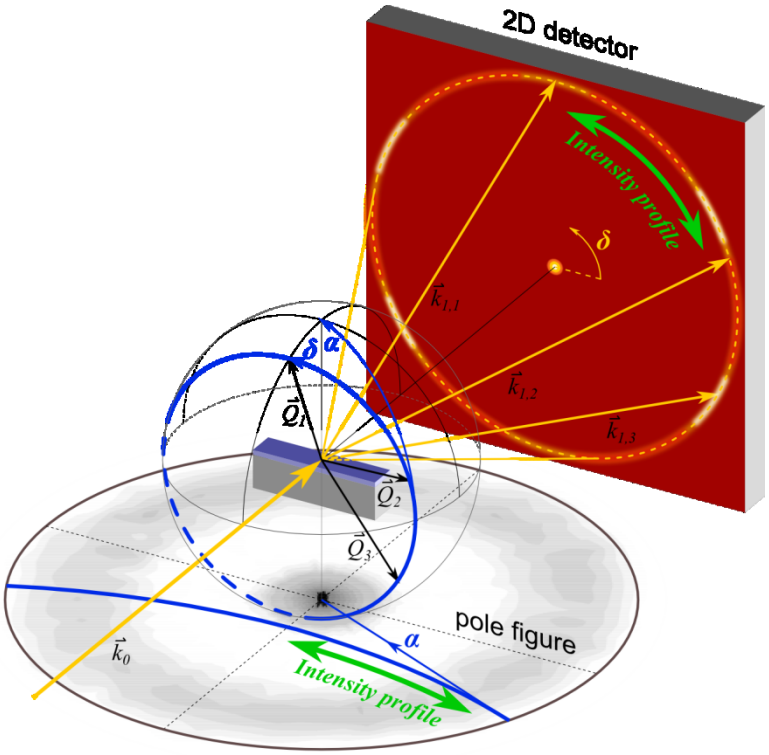

Fig. 2.7: Correlation between a 2D diffraction pattern and a pole figure. The diffraction signal from a Debye-Scherrer ring corresponds to diffraction vector directions within a segmental cut through the sphere of orientation space. This cut can be seen as a curved line in the pole-figure associated with the sample.

2.2.5. Residual Stress Analysis

Whereas in a laboratory the diffraction vector has to be tilted through $\psi = 90 - \alpha$ for a residual stress measurement, in synchrotron nanodiffraction the recorded 2D images already contain multiple tilt angles of the diffraction vector that go through δ. In the case of an equibiaxialy stressed coating, the $d(hkl)$ variation as a function of the azimuthal angle δ can be expressed as follows:

$$\frac{\partial d_\delta(hkl)}{\partial \cos^2 \delta} = \frac{S_2(hkl)}{2} \sigma_\parallel d_0(hkl) \tag{2.7}$$

Note that in comparison with eq. 2.4 a $\cos^2\delta$ term replaces the $\sin^2\psi$ term because $\psi = 0°$ lies perpendicular to the sample surface whereas $\delta = 0°$ lies parallel to the sample surface for the sample orientation depicted in Fig. 2.7. As before, this equation has to be solved for $\sigma_\parallel$:

$$\sigma_\parallel = \frac{\partial d_\delta(hkl)}{\partial \cos^2 \delta} \frac{2}{S_2(hkl)} \frac{1}{d_0(hkl)} \tag{2.8}$$

Qualitatively, strain can be seen in the 2D diffraction pattern as an elliptical distortion of Debye-Scherrer rings, where the eccentricity is a measure for the magnitude of first-order strain present in the sample. As in the laboratory, stress results from this method are averages over the volume irradiated by the X-ray beam.

2.3. Nanoindentation

In the thin film community it is of much interest to characterize mechanical material properties, but as the sample dimensions are in the micron range, it is necessary to employ techniques that operate on this length scale successfully. Nanoindentation is a further development of instrumented indentation, shrunk down to indentation depths of several 10 to several 100 nm and indentation forces in the µN and mN range. As typical thicknesses of thin film coatings are several microns, the maximal indentation depths have to be smaller by a factor of 10 in order to avoid contaminating measurements with mechanical influence from underlying substrate material.

During instrumented indentation an indenter tip made from a hard material, such as diamond, is pushed into the specimen and both penetration depth and necessary force are registered to record force-penetration curves. (Fig. 2.8) Because of the small dimensions and forces, one common setup is to mount a three-capacitor transducer as a force-generation and displacement-measurement device on an atomic force microscope (AFM) and use the latter to move the sample and indenter and to image the indented surface. The resolution of both instrument parts is high enough to warrant reproducible measurements on the small scale.

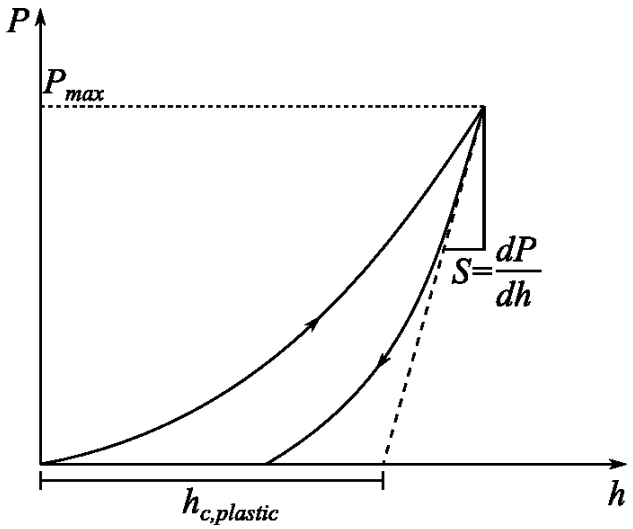

Fig. 2.8: Force-penetration curve recorded in a nanoindentation experiment. P_{max} is the maximum force exerted during the measurement, $h_{c,plastic}$ is the plastic contact depth at maximum force and S is the tangent at the beginning of the un-loading curve which is called *stiffness*.

Typical indenter tip shapes for testing of thin hard films are three-faced pyramids that are usually a cube corner or a so-called *Berkovich* pyramid which has an included angle of 142.35 ° between a face and an edge. This particular angle was chosen, so that the contact area of a Berkovich pyramid for a given depth is the same as for a Vickers indenter tip which is a four-faced pyramid that is used in the standardized Vickers indentation method for macroscopic samples.

From the force-penetration curve that is obtained during the measurement, two values can be calculated. The first is nanoindentation hardness which is defined as the maximum force exerted P_{max}, divided by the projected contact area of the indent at the maximum force A_c:

$$H = \frac{P_{max}}{A_c} \tag{2.9}$$

P_{max}can easily be extracted from the force-penetration curve, but the projected contact area usually has to be measured after the indentation with an AFM or in an optical microscope. Alternatively the projected contact area can be calculated from the corresponding contact depth h_c using a Taylor polynomial like

$$A_p(h_c) = C_0 h_c^2 + C_1 h_c^1 + C_2 h_c^{\frac{1}{2}} + \cdots \tag{2.10}$$

which is usually truncated after a few terms. $C_{0,1,2,\ldots}$ are constants that depend on the indenter tip shape and are fitted to data from a calibration measurement on a well known sample, typically fused silica. During the calibration data for A_p are calculated from the second value that is accessible through nanoindentation, which is the so-called *reduced Young's modulus*:

$$E_r = \frac{\sqrt{\pi}}{2} \frac{S}{\sqrt{A_p(h_c)}} \tag{2.11}$$

Here S is called stiffness and it is the gradient of the force-penetration curve at the moment of unloading. (Fig. 2.8) The reduced Young's modulus is a combined value that contains the elastic constants of the indented sample (index *s*) and the indenting tip (index *t*) which are known values when calibrating:

$$\frac{1}{E_r} = \frac{1-\upsilon_s^2}{E_s} + \frac{1-\upsilon_t^2}{E_t} \tag{2.12}$$

The determination of the stiffness from the force-penetration curve is commonly made by fitting the unloading curve with a general exponential function and then analytically computing the gradient at the point of unloading. This method was introduced by Oliver and Pharr in 1992 [22] and has proven to be robust for many indenter tip shapes and indentation conditions.

3. Experiments

3.1. Sample Preparation

Coatings deposited onto WC-Co cemented carbide cutting inserts were prepared by Böhlerit GmbH & Co. KG in Kapfenberg, Austria employing a low pressure chemical vapour deposition (LPCVD) process [8]. The complete coating system consists of a 5 µm $Ti_{0.05}Al_{0.95}N$ layer deposited on top of a 3.5 µm $TiC_{0.5}N_{0.5}$ hard layer and a 0.5 µm TiN bonding layer. Deposition conditions of the coating are listed in Tab. 3.1.

Individual coating samples were then annealed in ambient air for 1 hour at temperatures of 700 °C and 800 – 1150 °C in 50 °C steps. One sample was kept untreated as a reference for the as-deposited state.

Further reference samples were two other commercial coating systems that were annealed under the same conditions. These coatings were deposited by physical vapour deposition (PVD) using magnetron sputtering and arc evaporation [3, p.95ff]. Their respective compositions are TiAlN (40 % Ti to 60 % Al target ratio) and AlCrN (30 % Cr to 70 % Al target ratio). For deposition conditions see Tab. 3.1.

Tab. 3.1: Deposition conditions of the coatings studied in this work.

coating	layer	deposition temperature	deposition pressure
-	-	[°C]	[Pa]
LPCVD	TiN	900	$3 \cdot 10^4$
	$TiC_{0.5}N_{0.5}$	850	$1.2 \cdot 10^4$
	$Ti_{0.05}Al_{0.95}N$	800	$2.5 \cdot 10^3$
PVD (sputter) reference	TiAlN	500	$5.8 \cdot 10^{-1}$
PVD (arc) reference	AlCrN	450-500	2

A nanoindentation sample was prepared from the sample annealed at 1050 °C by focused ion beam (FIB) milling with a Zeiss AURIGA-CrossBeam workstation equipped with a Cobra-Orsay-Physics FIB that was also used for imaging as a scanning electron microscope (SEM) [11, p. 247ff]. In order to be able to obtain depth-resolved information on hardness, a lateral wedge-cut with a slope of 1:9 relative to the coating surface was made. (Fig. 3.9)

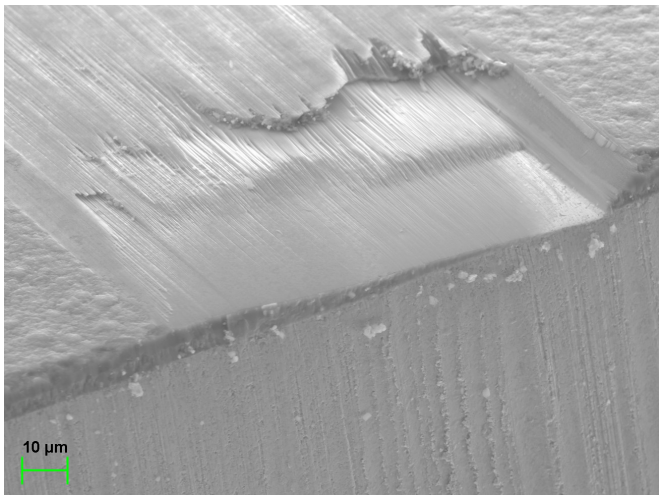

Fig. 3.9: Lateral FIB cut as a preparation for depth-resolved nanoindentation of the coating.

For microstructural analysis a cross-section of the sample annealed at 1100 °C was fabricated and examined by FIB milling, SEM imaging and energy dispersive X-ray spectroscopy (EDX) mapping. A part of the as-deposited sample was also prepared for high resolution transmission electron microscopy (HRTEM) performed in a Jeol 2100F microscope equipped with a C_s corrector that compensates for spherical aberration [9].

Samples for synchrotron cross-sectional X-ray nanodiffraction were prepared from an as-deposited sample and one annealed at 1050 °C by first cutting a thin section with a diamond wire saw, gluing it to a brass carrier ring and then further thinning the section by mechanical polishing. As the sample material is very hard, no considerable influence from this method of preparation on the measured properties is expected. The resulting sample thickness was below 100 µm.

3.2. XRD Laboratory Measurements

A 5-circle Rigaku SmartLab X-ray diffractometer was used to characterize phase compositions and to validate synchrotron residual stress measurements. (Fig. 3.10) On the primary side the X-ray source was a 1.5 kW sealed tube that generated Cu K_α radiation ($\lambda = 1.54 \cdot 10^{-10}$ m) with a line focus and a parabolic multi-layered mirror was used to parallelise the beam. Soller slits were used on both the primary and the secondary side and a scintillation detector with a flat carbon monochromator was employed. To increase resolution, a 0.5° parallel slit analyser was mounted on the detector arm after the first receiving slit [16, p.87ff].

Phase analysis was carried out with a grazing incidence of 1°, so that the measurement was very surface sensitive and only the $Ti_{0.05}Al_{0.95}N$ layer contributed to the diffraction signal. The scan range was from 25° to 90° in 2θ with a 0.05° step and a measurement speed of 2° per minute. The beam dimensions were 1 mm by 10 mm in order to obtain information from a large sample area.

Residual stress characterization was performed by measuring the TiCN 200 diffraction peak in a ψ range of 0-80° in 10 equidistant $\sin^2\psi$ steps. Resolution and measurement speed in 2θ were 0.03° and 6° per minute respectively.

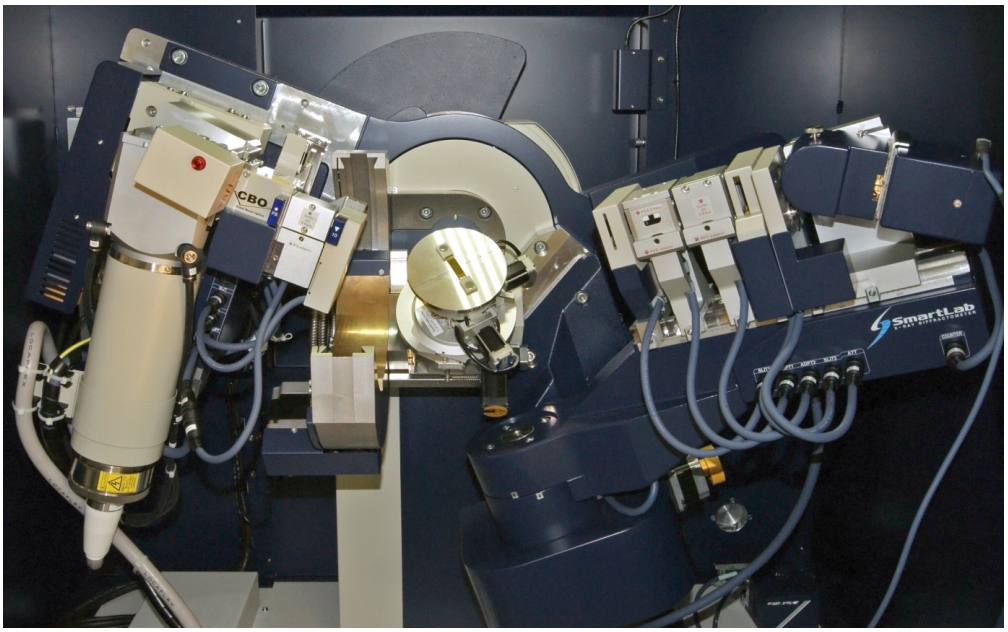

Fig. 3.10: Rigaku SmartLab 5-circle thin-film X-ray diffractometer used for phase analysis and residual stress measurements.

3.3. X-ray Nano-beam Characterization

Synchrotron XRD measurements were carried out at the nanofocus extension of the microfocus beamline ID13 of the ESRF (European Synchrotron Radiation Facility) in Grenoble, France. The beam was focused to a line with a width of 50 nm and a length of 2 µm. The coating was scanned across its cross-section with a step of 100 nm between diffraction pattern recordings (Fig. 2.3).

The beam energy was 14.9 keV ($\lambda = 0.832 \cdot 10^{-10}$ m), as adjusted by a two-bounce liquid-cooled single crystal monochromator in the beam pre-conditioning optics prior to the experimental station. The sample-to-detector distance was approximately 87 mm and it was further calibrated along with the detector misalignment by a LaB_6 standard calibration powder measurement.

The experimental setup gives the user precise control over the position of the sample relative to the beam through the use of a piezo-driven tripod and a retractable optical microscope that is aligned to the beam centre. (Fig. 3.11) Beam size and focus can be controlled by two Kirkpatrick-Baez mirrors and an edge-defining slit system just ahead of the sample. Pre-conditioning of the beam is necessary however, which is done along with the wavelength selection in the beamline optics system.

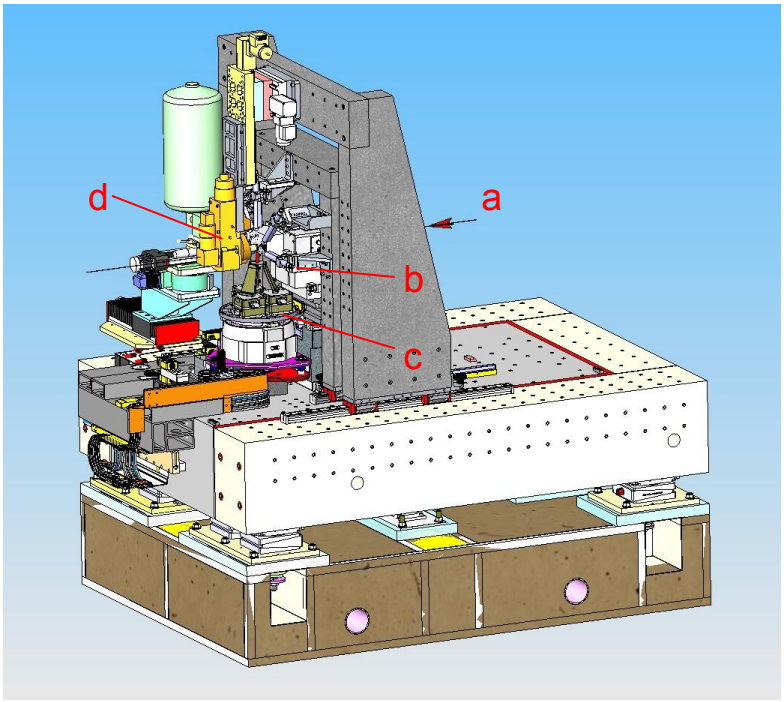

Fig. 3.11: A computer drawing of the experimental setup of the nanofocus end station at the ID13 beamline of the ESRF. The beam enters from the right along the red arrow (a) and is focused by a Kirkpatrick-Baez mirror system (b). The sample is mounted on a positioning and scanning stage (c) and is aligned relative to a retractable optical microscope that sits at the beam centre (d). All parts are mounted on a granite framework. Images are recorded by a 2D image plate detector with a resolution of 2048x2048 pixels (not shown). Adapted from [14].

Elastic constants used for residual stress evaluation are listed in Tab. 3.2. Values of fcc-$Ti_{0.05}Al_{0.95}N$ and $TiC_{0.5}N_{0.5}$ were interpolated for the appropriate composition. The standard deviation of calculated residual stress values is in the order of ± 10 %.

Tab. 3.2: X-ray elastic constants used for residual stress evaluation

$\frac{1}{2}S_2$ (w-AlN, 100)	$\frac{1}{2}S_2$ (fcc-TiAlN, 200)	$\frac{1}{2}S_2$ ($TiC_{0.5}N_{0.5}$, 200)	$\frac{1}{2}S_2$ ($TiC_{0.5}N_{0.5}$, 111)
[Pa^{-1}]	[Pa^{-1}]	[Pa^{-1}]	[Pa^{-1}]
$0{,}3931 \cdot 10^{-11}$	$0{,}5495 \cdot 10^{-11}$	$0{,}2439 \cdot 10^{-11}$	$0.2831 \cdot 10^{-11}$
[23]	[24]	[25-27]	[25-27]

3.4. Nanoindentation Experiment

For nanoindentation measurements, a Hysitron Triboscope transducer mounted on a Veeco Dimension 3100 atomic force microscope (AFM) was used. (Fig. 3.12) Indents were made with a Berkovich indenter tip approximately 6 µm apart on a slope that was previously laterally cut into the sample. (See chapter 3.1.) Therefore the in-depth resolution of the hardness measurements was approximately 0.7 µm.

For each lateral position corresponding to a distinct coating depth, 5 indents with varying loads were made in order to be able to recognize indentation size effects and a hardness increase due to ion implantation during FIB milling [11, p.13ff]. After the evaluation of measurement data and measurement errors due to non-linear mechanical effects such as pop-ins and surface roughness related phenomena [22], only the middle three loads of 5 mN, 7.7 mN and 10 mN were considered for final interpretation.

Furthermore the sample was tilted against the slope during the measurements, so that standard indentation conditions could be guaranteed. For this purpose, the sample was glued onto a steel wedge with the reversed slope of the lateral cut which is stiff enough to not influence the measurement. A simple calculation shows that at an indentation force of 10 mN the displacement of the sample due to elastic response from the reverse wedge is only 0.05 nm for the chosen sample size.

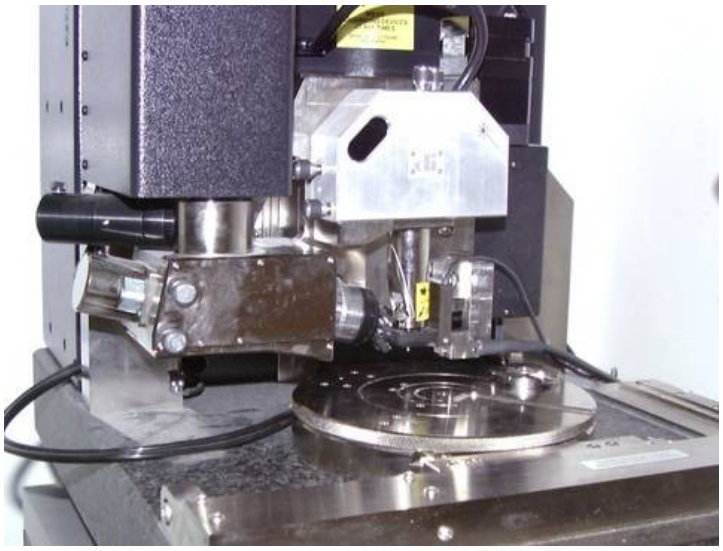

Fig. 3.12: Veeco Dimension 3100 atomic force microscope with Hysitron Triboscope transducer for nano-mechanical experiments.

4. Results and Discussion

4.1. Surface Changes After Oxidation

Already without the use of advanced characterization techniques it was evident after the annealing treatment for 1 hour in air that there are significant differences between the novel $Ti_{0.05}Al_{0.95}N$ coating and the two reference coatings (Fig. 4.13). These can be recognized when comparing the surface roughness of the LPCVD $Ti_{0.05}Al_{0.95}N$ coating and both PVD coatings. The CVD coating exhibits a relatively compact and smooth surface morphology even after oxidation at 1100°C (locally). This is particularly important because a smooth surface and good adherence to the substrate are critical for typical wear resistance applications of hard coatings.

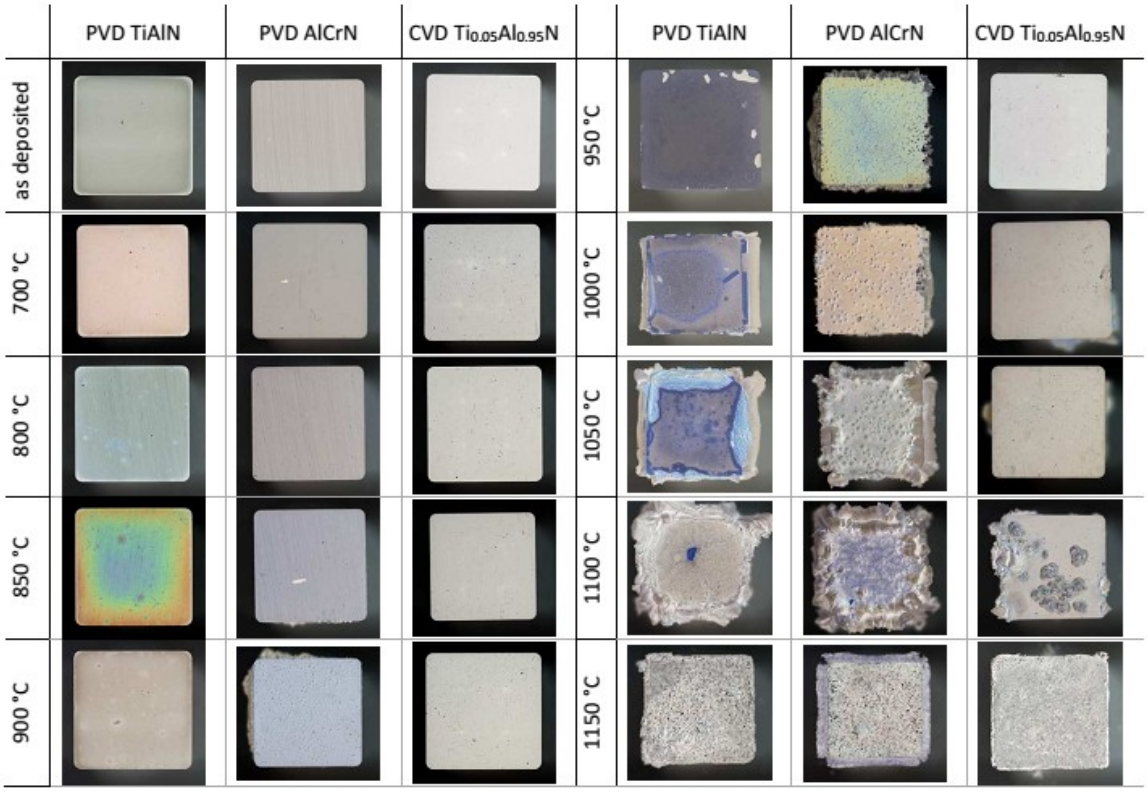

Fig. 4.13: Coating sample series annealed in ambient air for 1 hour at different temperatures. The LPCVD $Ti_{0.05}Al_{0.95}N$ coating outperforms both of the two PVD reference coatings in terms of both surface roughness and top-layer oxide formation by several 100 °C.

Furthermore differences in discolouration could be observed, which is indicative of the formation of top-layer oxides because of visible light interference phenomena in transparent thin oxide films. The PVD coatings began to heat-tint at 700 °C and 850 °C respectively whereas the CVD coating showed the first signs of discolouring only after annealing at 950 °C. This coincides with grazing incidence XRD phase analysis results presented in chapter 4.2, where the top layer oxide first could be observed at the same temperature.

Another point of interest is that the $Ti_{0.05}Al_{0.95}N$ coating resists oxidation so well, that the high temperature stability in fact seems to be limited by the substrate and not by the coating. This is deduced from the observation that at temperatures above 1100 °C the destruction of the coating is highly localised in the form of oxidation blisters that stem from the substrate material. (Fig. 4.14) However next to the sites where the coating was ruptured by rapid and violent oxidation of the underlying material, it was found to still adhere well and remained untouched by oxidation. Only at 1150 °C and above the coating oxidised in a manner that renders it unfit for further use (coating decohesion and delamination).

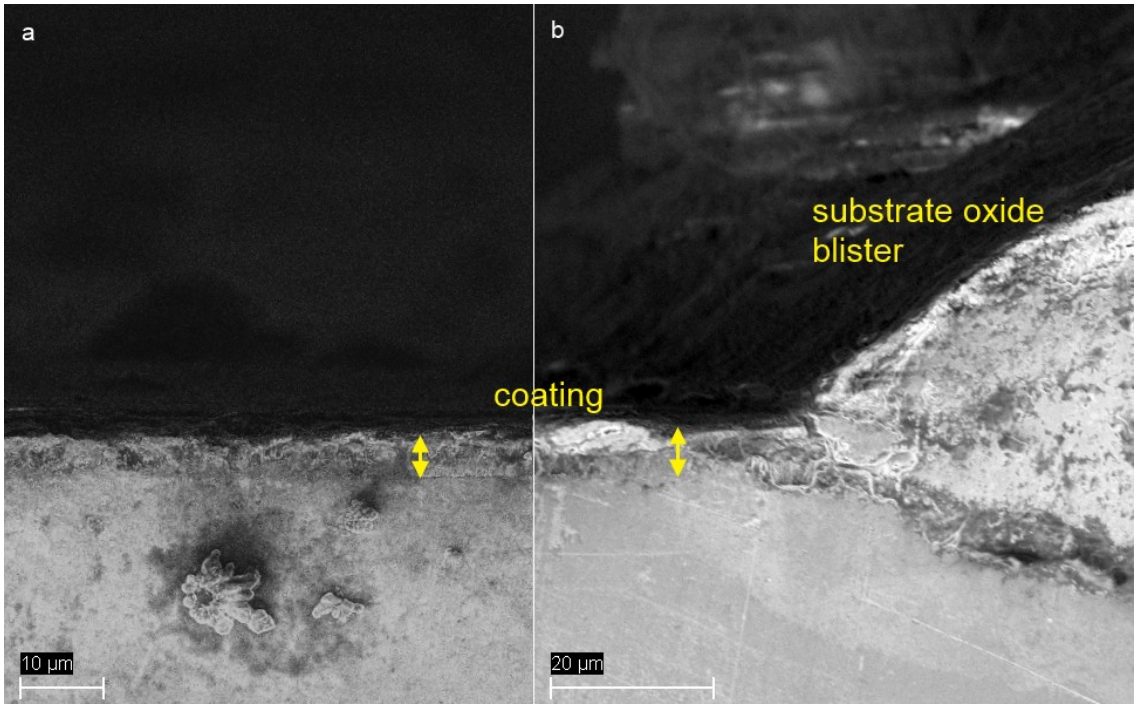

Fig. 4.14: Cross-sectional SEM image of a substrate oxidation blister site (b) on the sample annealed at 1100 °C. Directly beside the rupture (a) the coating remained intact and was found to still adhere well to the substrate. The distance between images (a) and (b) is approximately 1 mm.

4.2. Phase Analysis by Laboratory XRD in Grazing Incidence Geometry

Each of the samples from the annealing series underwent a phase analysis by laboratory XRD in surface sensitive geometry [16, p.186ff]. In Fig. 4.15 the depicted scan range was shortened to $2\theta = 25° - 47°$ in order to illustrate observations more clearly. Because the sample annealed at 1150 °C was oxidized completely and therefore was very rough, no meaningful measurement concerning phase composition could be performed. In order to identify phases coloured lines represent known peak positions of specific phases from a database (ICDD PDF-2 [28]) that are matched to the recorded pattern.

In the as-deposited state the phases in the topmost few microns include a cubic (fcc) TiAlN mixed phase and hexagonal or wurtzite (w) AlN.

Two important changes could be documented with rising annealing temperature:

- The formation of a protective (in terms of oxidation resistance) top layer of α-Al_2O_3 or *corundum*. This can be seen by the increasingly strong appearance of the corresponding peaks from temperatures of 950 °C onwards.
- The decomposition of the fcc-TiAlN mixed phase into w-AlN and cubic (fcc) TiN which started occurring at the same temperatures [7].

Other than that, some small amounts of other oxides containing Ti could be detected, indicated by very weak peaks at the corresponding positions. However, these are not expected to contribute to the oxidation resistance of the coating because they lack the density of corundum and do not prevent oxygen diffusion as well [29].

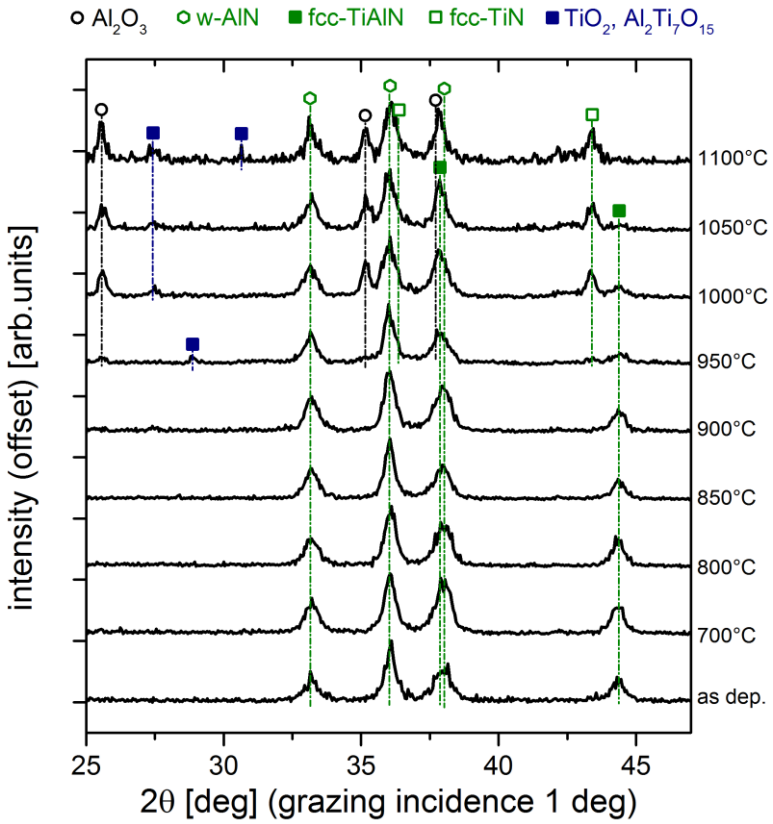

Fig. 4.15: Phase analysis by laboratory XRD revealed the formation of a protective α-Al_2O_3 top layer and the decomposition of cubic (fcc) mixed phase TiAlN into wurtzite (w) AlN and cubic (fcc) TiN. Trace amounts of other oxides containing Ti could also be detected.

It is believed that the very high Al content of the $Ti_{0.05}Al_{0.95}N$ layer facilitates the diffusivity and availability of Al for the formation of the protective oxide layer which itself is a well-known and effective diffusion barrier for oxygen. This is probably the main reason for the very good oxidation resistance of the CVD coating.

The formation of substrate material oxidation blisters, which is the limiting phenomenon in terms of high temperature stability in oxidative environments, could be attributed to the sporadic appearance of higher concentrations of parasitic Ti-containing oxides. These can provide diffusion paths for oxygen into the substrate, so that oxidation can occur locally. Substrate oxidation is accompanied by a volume increase which further corrupts the protective abilities of oxides, for example by enlarging pores. Ultimately this leads to rapid

and violent oxidation that manifests in blisters that burst through otherwise unaffected coating material.

4.3. Microstructural Examination by Electron Microscopy

A FIB-milled cross-sectional micrograph of the sample annealed at 1100 °C revealed the grain size and morphology of the coating sub-layers [11, p.250ff]. (Fig. 4.16) The TiN bonding layer that is deposited first shows very fine grains, whereas the next hardness-enhancing $TiC_{0.5}N_{0.5}$ layer has comparatively coarse columnar grains. In the $Ti_{0.05}Al_{0.95}N$ sublayer of the coating the composite nature of this layer and angular grains with sizes between approximately 150 nm and 400 nm could be observed. The naturally grown oxide top layer could be seen as well as a protective Pt film that was deposited locally onto the sample in the FIB workstation prior to ion beam milling in order to protect the sample from deteriorating during preparation [11, p.53ff]. Discontinuities in the oxide layer and horizontal cracks near the coating surface can be attributed to a previous sample preparation step where a comparatively coarse cut was made with a tabletop cut-off machine. The depicted cross-section was recorded in proximity to this cut and therefore the visibility of some preparation artefacts could not be avoided.

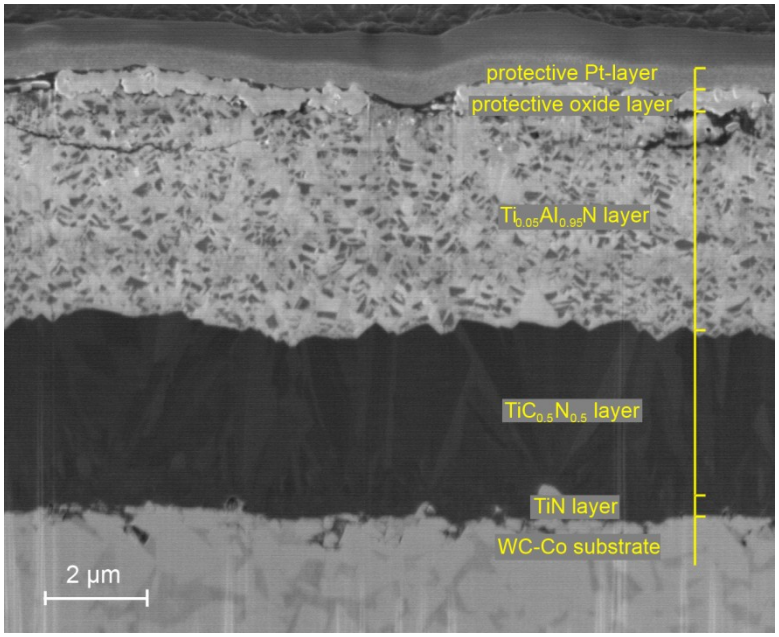

Fig. 4.16: SEM micrograph of the $Ti_{0.05}Al_{0.95}N$ based coating cross-section shows the individual sub-layers and their morphology. Gaps in the oxide layer and horizontal cracks are due to sample preparation.

An EDX mapping [10, p.179ff] performed on the area imaged above resolved and confirmed the chemical composition of the respective layers as they are denoted in the micrograph image and described in chapter 3.1. (Fig. 4.17) A certain amount of carbon was detected not only in the $TiC_{0.5}N_{0.5}$ layer, but also in the rest of the mapped area, but this is due to carbon deposition during scanning with an electron beam which is a known issue of SEM imaging [10, p.70ff].

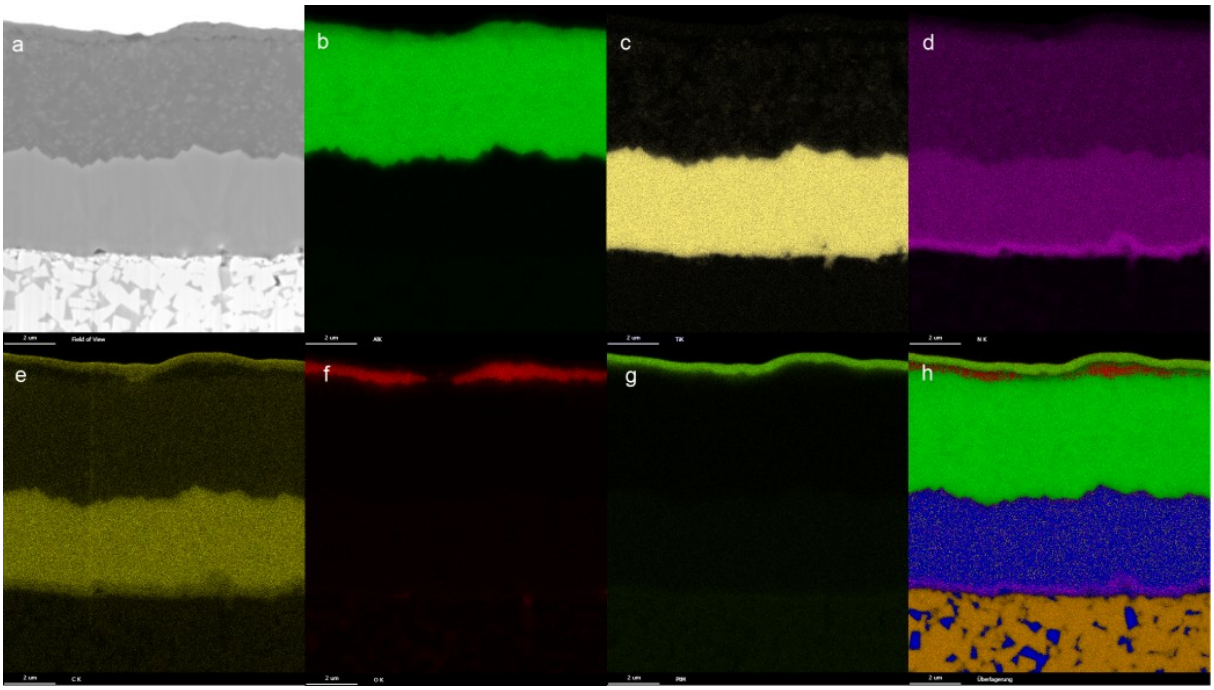

Fig. 4.17: EDX mapping on the area of the micrograph: (a) field of view; (b) Al; (c) Ti; (d) N; (e) C; (f) O; (g) Pt; (h) composite of all mappings, including Co and W which are found in the substrate. Carbon can be seen throughout the sample because of carbon deposition during SEM imaging.

In order to gain more insight into the microstructure of the $Ti_{0.05}Al_{0.95}N$ layer a TEM lamella was prepared from the sample used in the SEM. (Chap. 3.1) It was studied by TEM imaging, selected area diffraction (SAD) which is electron diffraction in an appropriate electron microscope, EDX and high resolution TEM imaging [9].

The thickness of the protective oxide Al_2O_3 top layer was measured and found to be between 300 nm and 400 nm for the given oxidation conditions of 1 hour in ambient air at 1100 °C. (Fig. 4.18) The original layer and its oxide have a very good interconnection which corresponds to the excellent adherence that corundum is known for.

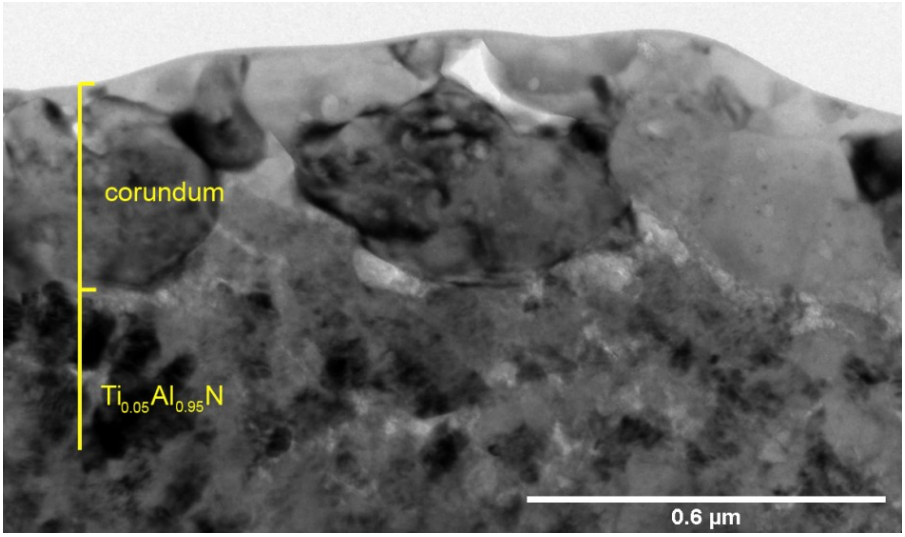

Fig. 4.18: TEM image of the protective oxide top layer on the coating sample annealed at 1100 °C. Its thickness is approximately 300 nm to 400 nm.

It was discovered that, in the as-deposited $Ti_{0.05}Al_{0.95}N$ sub-layer, w-AlN and fcc-TiN precipitate in a lamellar nanocomposite microstructure with lamellar thicknesses of 10 nm and 3 nm respectively. The respective phases were identified by SAD and EDX. Packets of these lamellae reach a size of a few 100 nm and are oriented randomly inside the coating. (Fig. 4.19) To the author's knowledge this is the first coating of the TiAlN type where such a self-organised lamellar microstructure was observed.

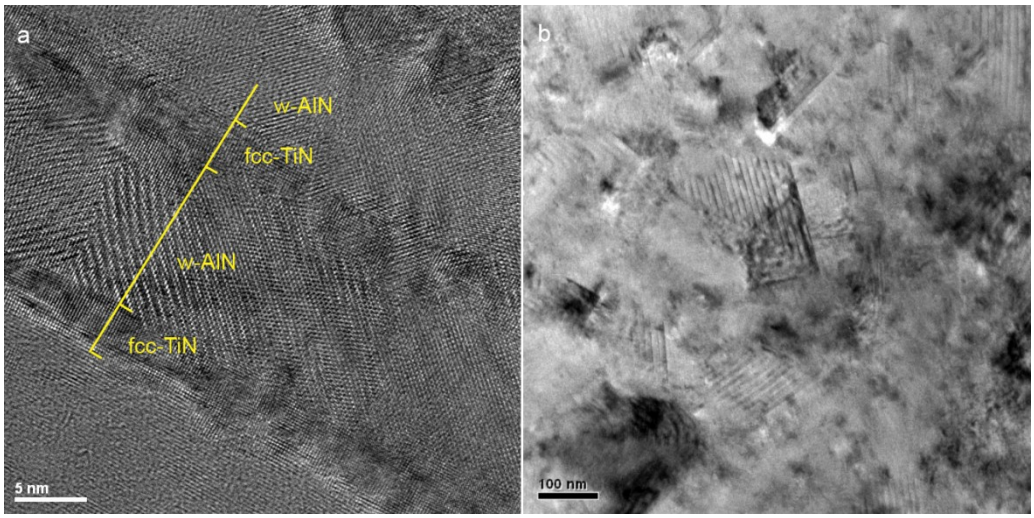

Fig. 4.19: HRTEM images of the lamellar nanocomposite microstructure found inside the as-deposited $Ti_{0.05}Al_{0.95}N$ layer. Lamellar packets have an interlamellar spacing of 3 nm and 10 nm for w-AlN and fcc-TiN respectively (a) and are randomly oriented with respect to each other (b).

The unusual microstructure of the $Ti_{0.05}Al_{0.95}N$ layer affects its mechanical properties considerably and thus also benefits the overall coating properties [30, p.348ff]. (See chap. 4.5)

4.4. Synchrotron Nanodiffraction Measurements

4.4.1. Depth-resolved Phase Analysis

Depth-resolved transmission XRD measurements with a very narrow beam at a synchrotron facility verified phase compositions determined from laboratory XRD (Chap. 4.2) and EDX mapping (Chap. 4.3) and revealed additional information on preferred orientations and residual stress gradients [12, 13].

First, azimuthally integrated two-dimensional (2D) data (Chap. 2.2.3) were used to obtain plots where the phase composition at a specific depth within the coating could be evaluated. (Fig. 4.20) Here the formation of the protective oxide top layer and the decomposition of the fcc-TiAlN mixed phase into w-AlN and fcc-TiN could be documented again. Additionally it was possible to determine that there is no apparent depth-gradient of the sublayer composition.

The boundary between the $Ti_{0.05}Al_{0.95}N$ and the $TiC_{0.5}N_{0.5}$ layer in Fig. 4.20 is smeared due to the facts that it is jagged (Fig. 4.15) and that the beam had a length of 2 µm along the

boundary direction. Moreover the TiN bonding layer peaks are not visible in Fig. 4.20 (a) due to the very high intensity of the $TiC_{0.5}N_{0.5}$ peaks which made it necessary to choose an intensity scaling range where the weak peaks from the nanocrystalline TiN layer are not differentiable from the background intensity level.

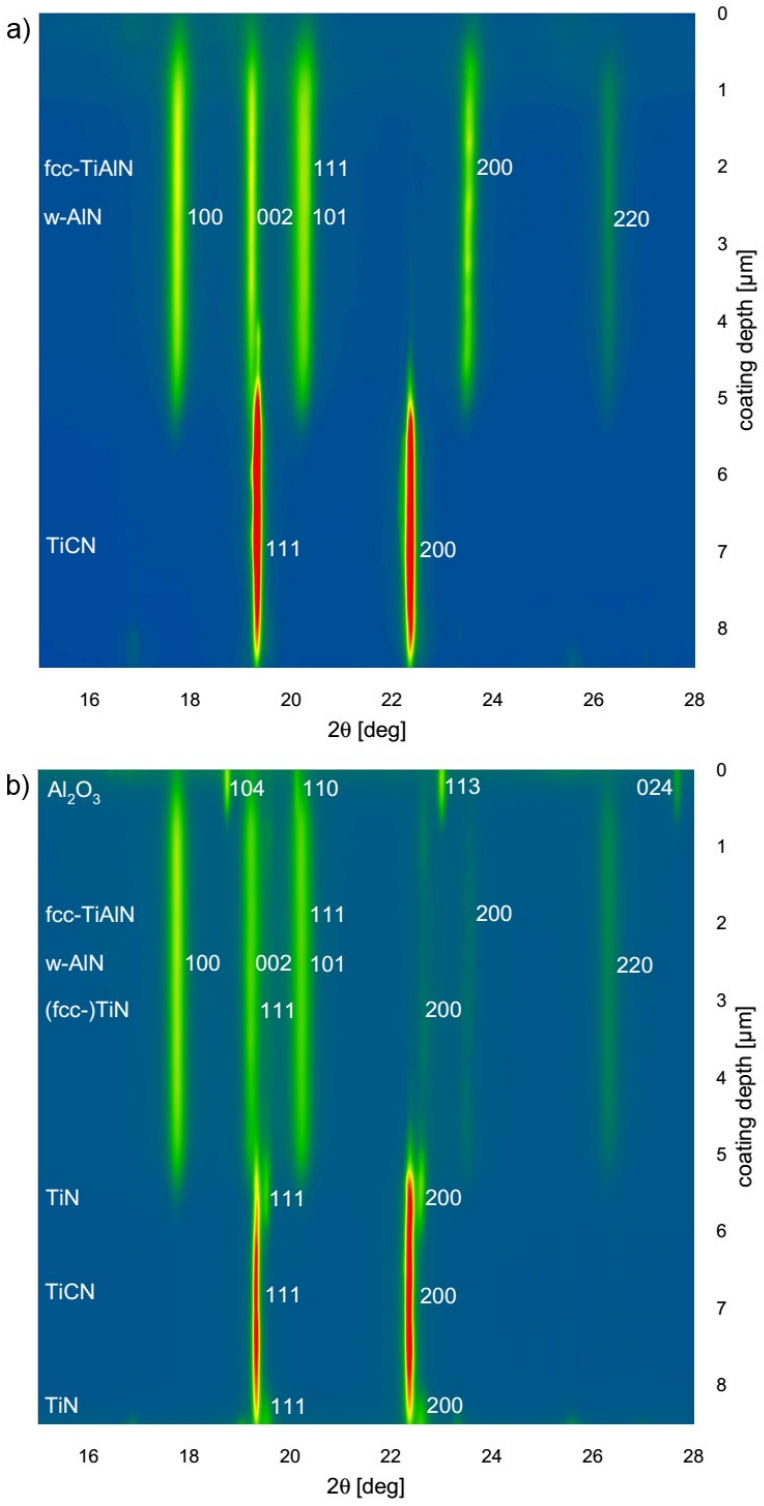

Fig. 4.20: Powder diffraction patterns evaluated from 2D diffraction data and plotted with their respective depth in the coating along the ordinate of a graph where intensity is coded as colour ranging from blue to red. Phases and their diffraction peaks are indicated next to the corresponding peaks in the graph. As-deposited (a) and oxidized at 1050 °C in air for 1 hour (b) states are shown.

4.4.2. Depth-dependent Crystallographic Texture Evaluation

Due to the coarse-grained nature of the $TiC_{0.5}N_{0.5}$ layer there were comparatively few grains that were irradiated by the incident X-ray beam and contributed to the diffraction pattern. For this reason the corresponding Debye-Scherrer rings became non-continuous and more or less discrete diffraction spots of single grains could be seen. This also means that a texture analysis (chap. 2.2.4) could not be made properly for this layer. At best, an educated guess is possible that there is no apparent preferred orientation present in this sub-layer.

Examination of peak intensity distributions in the $Ti_{0.05}Al_{0.95}N$ layer revealed a weak {001} fibre texture of w-AlN and no preferred orientation of the fcc-TiAlN mixed phase in the as-deposited sample. (Fig. 4.21)

In the sample annealed at 1050 °C the w-AlN phase showed no change but the in fcc-TiAlN mixed phase two layers of different texture can be seen. (Fig. 4.22) Near the surface a very weak {111} fibre texture developed whereas near the underlying layer it is a weak {112} fibre texture. Moreover the fcc-TiN phase that is a product of the decomposition of fcc-TiAlN was randomly oriented. At the interface between the $Ti_{0.05}Al_{0.95}N$ and $TiC_{0.5}N_{0.5}$ layer there is some interference from the underlying layer visible because of the proximity of the TiN and TiCN diffraction peaks and the layer boundary smearing mentioned in the previous chapter. However this has no influence on the texture evaluation of the fcc-TiN phase.

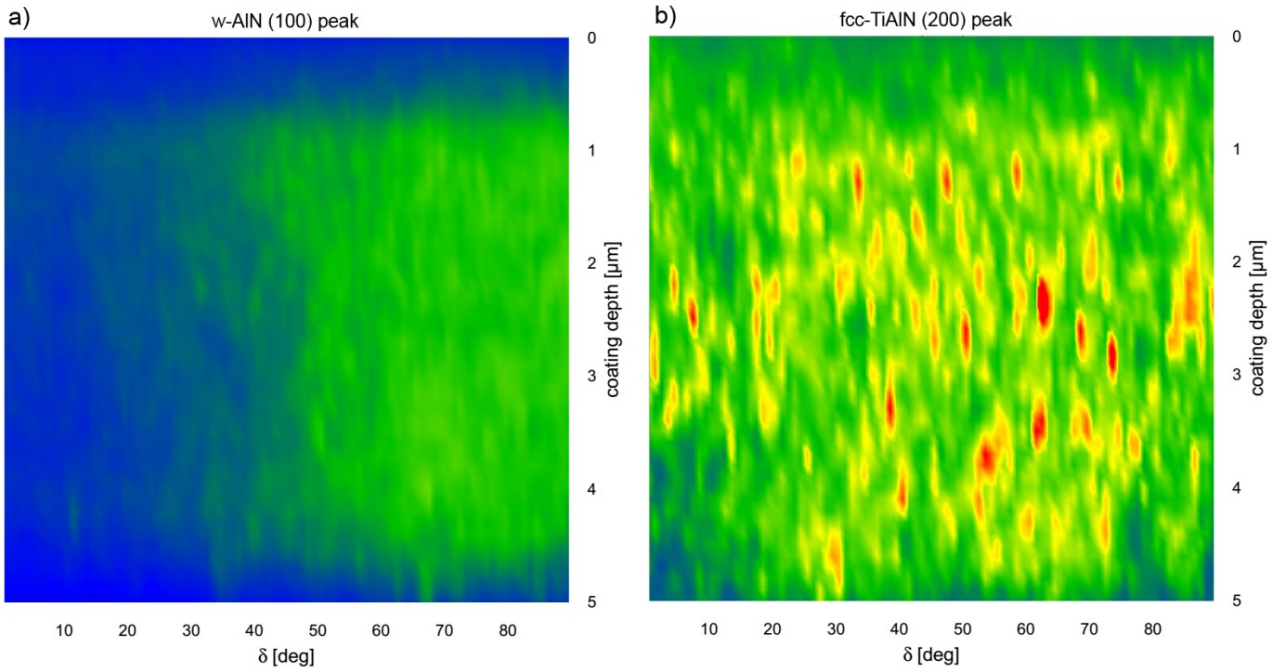

Fig. 4.21: Texture evaluation plots of the as-deposited sample. Diffraction intensities are shown colour-coded ranging from blue to red in dependence on their direction (azimuth angle δ) and their respective depth within the coating. Only phases in the $Ti_{0.05}Al_{0.95}N$ layer are included. A weak {001} fibre texture of w-AlN can be deduced (a) and no preferred orientation of fcc-TiAlN is discernible (b).

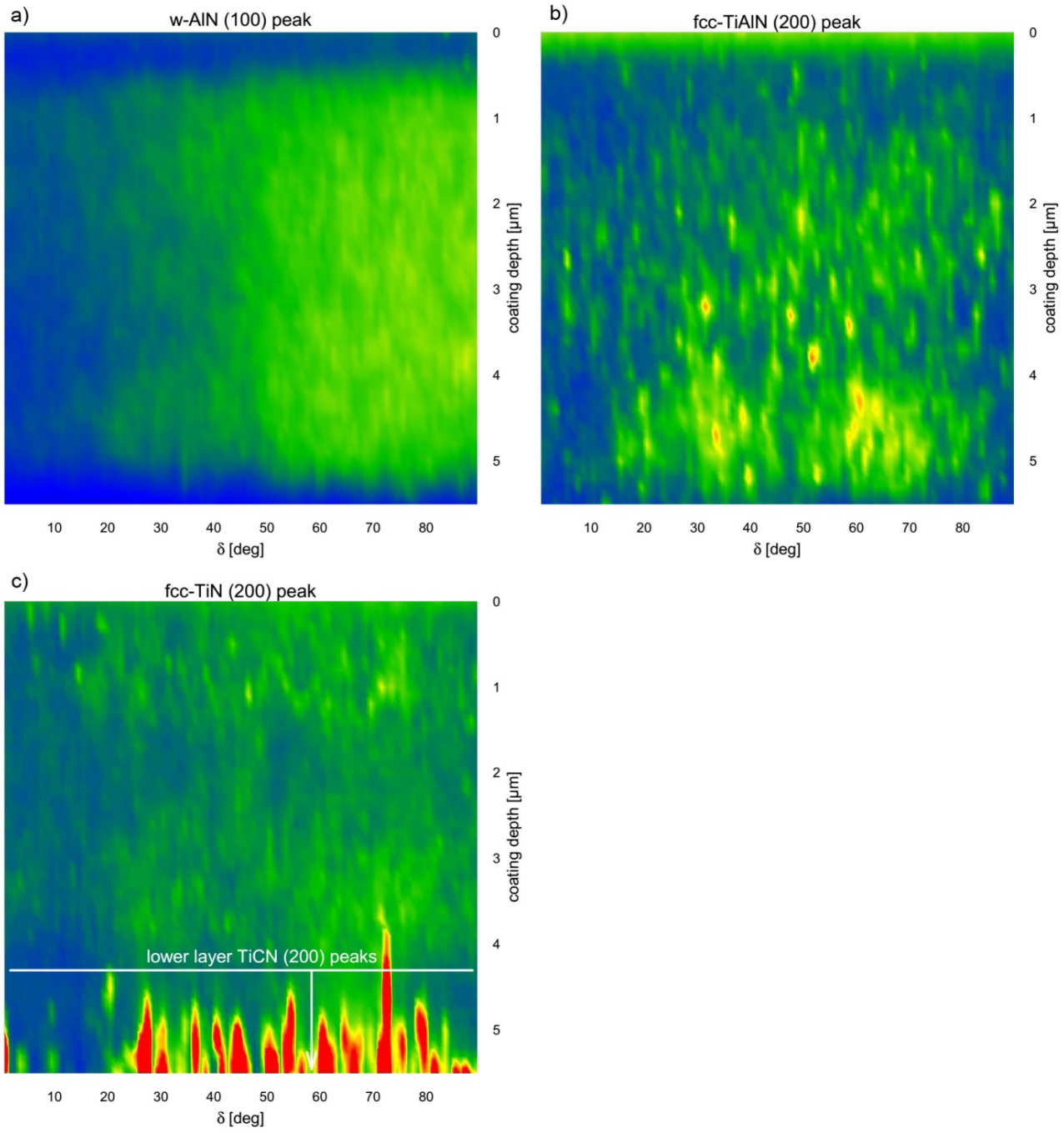

Fig. 4.22: Texture evaluation plots of the sample annealed at 1050 °C. Diffraction intensities are shown colour-coded ranging from blue to red in dependence on their direction (azimuth angle δ) and their respective depth within the coating. Only phases in the $Ti_{0.05}Al_{0.95}N$ layer are included. A weak {001} fibre texture of w-AlN can be deduced (a) and no preferred orientation of fcc-TiN is apparent (c). The fcc-TiAlN mixed phase shows a very soft {111} fibre texture at the surface and a soft {112} fibre texture below that (b). Because of the proximity of TiN and TiCN diffraction peaks there are intrusions of the fcc-TiCN signal visible in (c) at the bottom of the image.

4.4.3. Depth-resolved Residual Stress Evaluation

By quantifying the elliptical distortion of Debye-Scherrer rings using the method described in chap. 2.2.5 it is possible to evaluate the X-ray elastic strain at a specific depth in the coating

sample. In order to obtain residual stress by this method it is necessary to use the appropriate X-ray elastic constants of the material and to assume a stress-free spacing for the chosen lattice planes. (See Tab. 3.2) This was done by first calculating depth-dependent strains and locating a depth range of minimal strain. In this depth-range the lattice spacing was averaged and used as an approximate value. Calculations show that the maximum error made by choosing an approximate stress-free lattice spacing from within the range of all measured spacings is well below 0.5 % and thus smaller than other error influences [17, p.122].

Residual stresses were evaluated for the as-deposited state and annealed at 1050 °C state considering the $Ti_{0.05}Al_{0.95}N$ and $TiC_{0.5}N_{0.5}$ layers. For this purpose the diffraction rings corresponding to w-AlN (100), fcc-TiAlN (200), TiCN (200) and TiCN (111) were used. Peak positions were fitted in 36 10°-wide circular sections of each Debye-Scherrer ring and subsequently employed in the $\sin^2 \delta$ linear regression. (See chap. 2.2.5)

The results of the analysis in the $Ti_{0.05}Al_{0.95}N$ sublayer show a strong compressive residual stress at the coating surface that exponentially declines towards the substrate. (Fig. 4.23) After annealing the stress gradient relaxes and the average stress level increases which can be attributed to the decomposition of the fcc-TiAlN mixed phase into w-AlN and fcc-TiN which effectively represents an *age hardening* of the layer [31]. Because there is scarcely any fcc-TiAlN phase left in the annealed sample the calculated stress level shows comparatively larger fluctuations which are due to low diffraction intensities. (See Fig. 4.20)

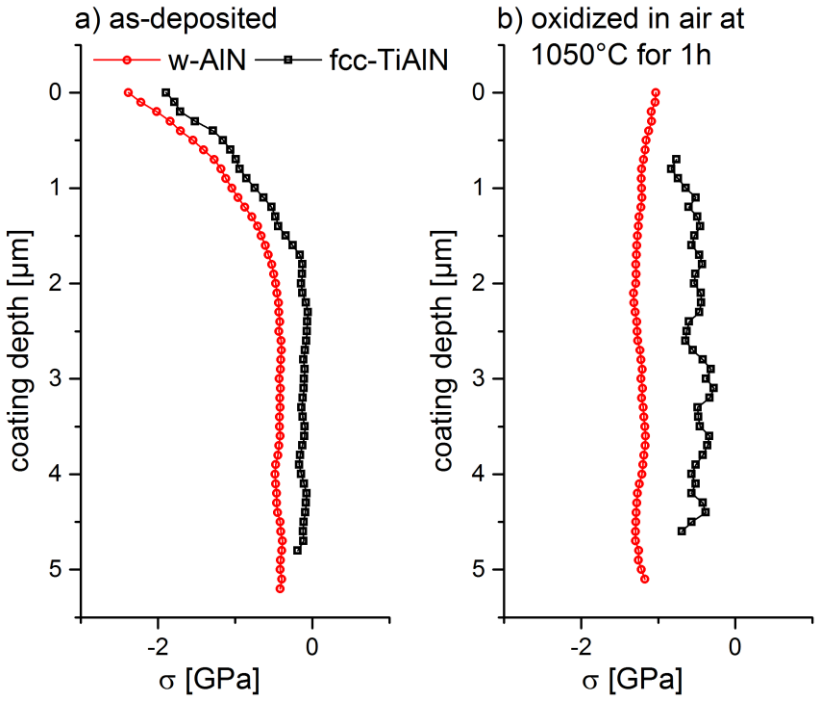

Fig. 4.23: Residual stress profiles across the $Ti_{0.05}Al_{0.95}N$ layer in the as-deposited and annealed samples. A relatively high compressive stress state at the surface decreases exponentially towards the substrate (a) and relaxes during annealing (b). This is superimposed by a stress increase that is caused by the phase decomposition of fcc-TiAlN into w-AlN and fcc-TiN [31]. Because there is almost no fcc-TiAlN left after annealing there are comparatively larger fluctuations of the corresponding stress level visible. This is due to very low diffraction intensities that make peak position fitting less reliable.

In the $TiC_{0.5}N_{0.5}$ layer an almost constant tensile residual stress profile could be measured, which increases slightly after annealing. (Fig. 4.24) This could be explained by considering the mechanical balance of the coating, where a greater compressive stress in the upper layer must lead to a greater tensile stress in the lower layer. In support of this explanation a small gradient of tensile stress can be seen in the annealed sample stress profile near the layer interface.

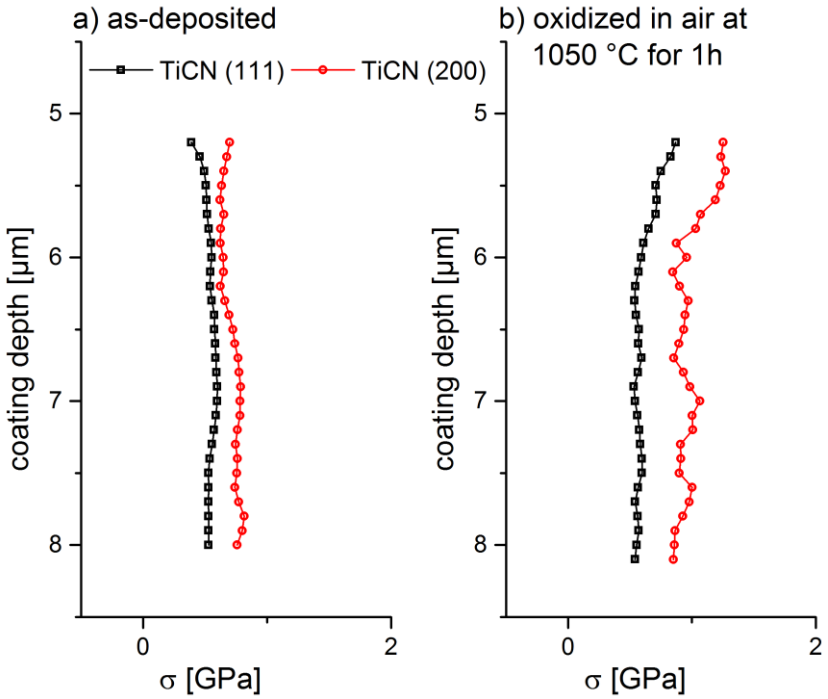

Fig. 4.24: Residual stress profiles of the $TiC_{0.5}N_{0.5}$ layer before and after annealing show an almost homogeneous distribution of tensile stress (a) that slightly increases after the treatment (b). This can be explained by mechanical balancing with the overlying layer which is also indicated by a minor stress gradient toward the layer interface in the annealed sample.

In order to verify stresses measured by synchrotron nanodiffraction the volume-averaged residual stress of the $TiC_{0.5}N_{0.5}$ layer in the as-deposited sample was measured by laboratory XRD. The value obtained from this method of 1.1 GPa ± 0.14 GPa was also in the tensile range, but about 30 % higher which can be attributed to the error margin inherent to XRD stress measurements on the one hand and to simultaneous measurement of the TiN layer along with TiCN in the laboratory diffractometer. This is due to the small difference in lattice spacing between those layers which leads to very close diffraction peaks that might even blend into one peak when the whole coating is irradiated by the X-ray beam.

4.5. Nanoindentation

Results from mechanical testing by means of nanoindentation (see chap. 2.3) on the sample annealed at 1050 °C revealed the depth-dependent hardness and elastic modulus profile of the coating system. Indents were made with varying loads on a sloped section of the coating and evaluated with the Oliver and Pharr method in order to obtain this information. (See chap. 3.4 and [22])

At the employed load levels of 5 mN, 7.7 mN and 10 mN the penetration depths were a multiple of the thickness of the FIB milling influenced layer [11, p.13ff], which is why there should not be any artificial increase in measured hardness values. Furthermore and as anticipated for hard ceramic coatings no indentation size effect [30, p.348ff] was observed.

The two main layers, $Ti_{0.05}Al_{0.95}N$ and $TiC_{0.5}N_{0.5}$, could be distinguished because of their different hardness level which was approximately 29 GPa and 36 GPa respectively. (Fig. 4.25) Part of this was surprising because TiAlN layers with very high w-AlN content are expected to be softer.

However it has already been observed that multi-phase layers with a nanocomposite structure show a strong hardness increase compared to their single-phase counterparts with the same chemical composition. Moreover investigations into synthetic periodic multi-layered coatings have suggested that a lamellar structure is also beneficial to the mechanical properties of the overall coating. Thus the nano-scale multi-phase lamellar microstructure of the LPCVD $Ti_{0.05}Al_{0.95}N$ layer can be assumed to be the cause for the observed exceptional hardness [30, p.78ff].

This means a significant improvement for coating performance in application because the high Al content that is necessary for good oxidation resistance until now has usually meant a trade-off in means of coating hardness. Further research into fine-tuning of the lamellae period might bring about even better hardness and promises to be an interesting topic for further studies.

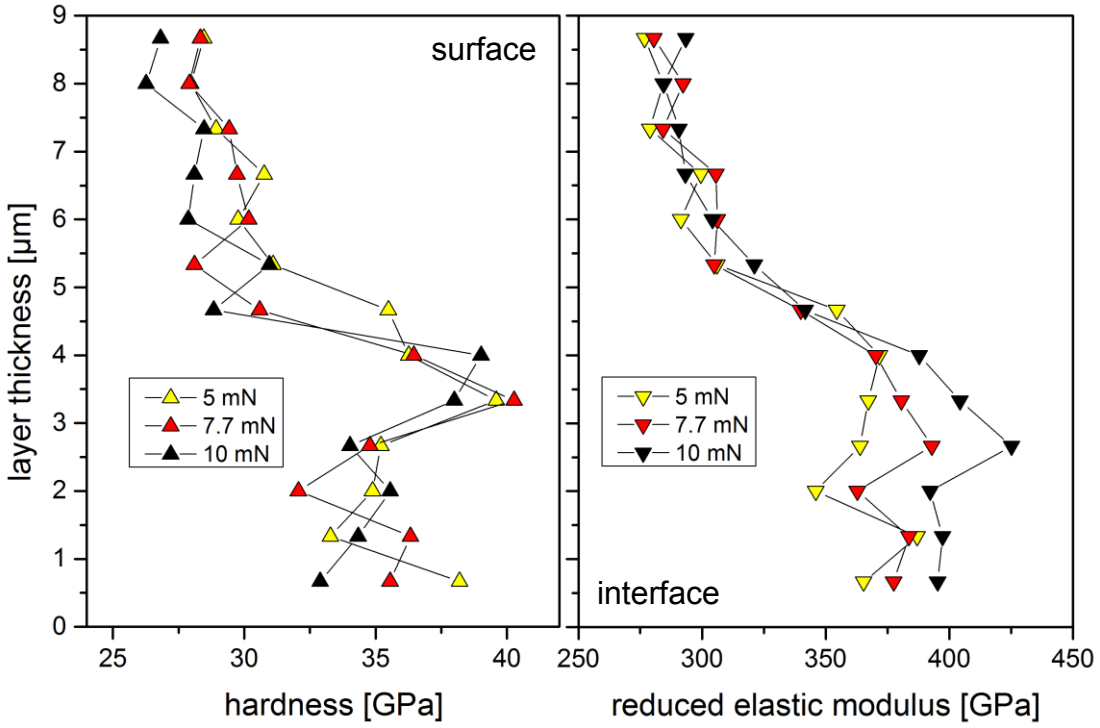

Fig. 4.25: Nanoindentation results showing depth-resolved layer hardness and elastic modulus. The $Ti_{0.05}Al_{0.95}N$ layer and the $TiC_{0.5}N_{0.5}$ layer can be distinguished by their differing level of hardness and reduced elastic modulus. Another point of interest is the comparatively high hardness of the $Ti_{0.05}Al_{0.95}N$ layer of approximately 29 GPa which is attributed to the formation of the self-organised lamellar microstructure found therein.

5. Summary

Structural and mechanical properties of a novel $Ti_{0.05}Al_{0.95}N$ coating prepared by low pressure chemical vapour deposition were investigated in as-deposited state and after annealing for 1 hour at varying temperatures in ambient air. The complete coating system consists of a 0.5 µm TiN bonding layer, a 3.5 µm intermediate $TiC_{0.5}N_{0.5}$ hard layer and a 5 µm $Ti_{0.05}Al_{0.95}N$ multi-phase top layer. The oxidation resistance was determined in form of an operating temperature limit and the oxidation behaviour was compared with two other coatings that are manufactured by different physical vapour deposition processes and are in common use for industrial applications.

Results comprehensively illustrated the superiority of the studied coating by showing that formation of surface oxides only started at 950 °C and the coating then remained intact until 1050 °C which is in both cases several 100 °C higher than for the reference coatings. It was observed that the temperature limit during oxidation of $Ti_{0.05}Al_{0.95}N$ is predetermined by the formation of substrate material oxidation blisters that burst through the coating, rupturing it locally. Directly next to these the coating remained intact until even higher temperatures and was ultimately completely oxidized from 1150 °C onwards.

Microstructural examination of the coating by electron microscopy methods such as scanning electron microscopy (SEM), transmission electron microscopy (TEM), high resolution TEM, selected area diffraction (SAD) and energy dispersive X-ray spectroscopy (EDX) showed the morphology and chemical composition of the individual sub-layers of an oxidized sample (annealed at 1050 °C) and the as-deposited sample. The natural protective oxide layer that forms during annealing was found to be very dense α-Al_2O_3 (corundum) and to adhere well to the coating. Overall chemical composition of the other coating layers could be confirmed qualitatively and the measured individual thicknesses matched the values from the deposition recipe.

The TiN bonding layer is very fine-grained with grain sizes below the resolution limit of the recorded SEM images at the chosen magnification. The hard TiCN layer exhibited a comparatively coarse-grained columnar microstructure and the TiAlN layer showed angular grains with a size between those of the other two layers. High resolution imaging revealed the thickness of the protective oxide layer of 300 – 400 nm for the given oxidation conditions and led to the discovery of a nanoscale self-organized lamellar microstructure in the TiAlN layer. Lamellar packets are composed of cubic (fcc) TiN and wurtzite (w) AlN and reach sizes of a few 100 nm. They have a bi-layer period of 3 nm and 10 nm respectively and are oriented randomly.

Phase analysis by surface-sensitive X-ray diffraction (XRD) in the topmost layer documented the formation of a protective oxide top-layer and the decomposition of the cubic (fcc) TiAlN mixed phase into w-AlN and fcc-TiN from 950 °C onwards. Trace amounts of Ti-containing oxides were found and can possibly be used to explain the failure mode of the coating during oxidation.

Cross-sectional X-ray nanodiffraction was employed to obtain depth resolved information on phase composition, preferred orientation and residual stress. The results are in agreement with laboratory XRD and electron microscopy investigations mentioned above. Very weak fibre textures were found in the w-AlN phase ({001} type) and the fcc-TiAlN phase ({111} and {112} type). Other phases could not be evaluated due to insufficient grain statistics.

Stress profile analysis showed a graded compressive stress state in the $Ti_{0.05}Al_{0.95}N$ layer and a homogeneous tensile stress state in the $TiC_{0.5}N_{0.5}$ layer. Particularly interesting is the strong near-surface compressive stress of the $Ti_{0.05}Al_{0.95}N$ layer that is similar to a stress profile resulting from shot-peening. Upon annealing at 1050 °C this gradient relaxed into a homogeneous stress state and increased on average due to the volume increase associated with the phase decomposition of the fcc-TiAlN mixed phase. In order to maintain mechanical balance the tensile stress level of the TiCN layer increased slightly. The measured values were also validated by a laboratory XRD residual stress measurement.

Depth-resolved nanomechanical testing by indentation revealed a comparatively high hardness of the $Ti_{0.05}Al_{0.95}N$ layer which is unusual for very high Al contents and the subsequent high volume fraction of w-AlN. However this could be explained by the particular nanolamellar microstructure of this layer, as previous research suggests that nanocomposite and lamellar morphology is beneficial for the mechanical performance of hard coatings.

Summarizing, the exceptional oxidation resistance can be attributed to the high Al content of the coating. Furthermore a new nanoscale composite lamellae microstructure was discovered that forms under the novel low pressure CVD production process conditions. It was found to have a positive effect on the coating hardness. High hardness and oxidation resistance are very important factors for many applications and a combination of both would increase application performance greatly.

By tuning the deposition parameters the bi-layer period of the lamellar phase probably could be optimized for even better hardness while maintaining oxidation properties which promises to be an interesting topic for further studies.

6. Table of Figures

7. References

[1] J.H. Hsieh, A.L.K. Tan, and X.T. Zeng. Oxidation and wear behaviors of Ti-based thin films. *Surface and Coatings Technology*, 201(7):4094 – 4098, 2006.

[2] D. McIntyre, J. E. Greene, G. Hakansson, J.-E. Sundgren, and W.-D. Munz. Oxidation of metastable single-phase polycrystalline $Ti_{0.5}Al_{0.5}N$ films: Kinetics and mechanisms. *Journal of Applied Physics*, 67(3):1542–1553, 1990.

[3] M. Ohring. *Materials Science of Thin Films - Deposition & Structure*. Academic Press, 2nd edition, 2002.

[4] A. Horling, L. Hultman, M. Oden, J. Sjolen, and L. Karlsson. Mechanical properties and machining performance of $Ti_{1-x}Al_xN$-coated cutting tools. *Surface and Coatings Technology*, 191(2-3):384–392, 2005.

[5] P. H. Mayrhofer, D. Music, and J. M. Schneider. Influence of the Al distribution on the structure, elastic properties, and phase stability of supersaturated $Ti_{1-x}Al_xN$. *Journal of Applied Physics*, 100(9):5, 2006.

[6] G. Erkens, R. Cremer, T. Hamoudi, K.-D. Bouzakis, I. Mirisidis, S. Hadjiyiannis, G. Skordaris, A. Asimakopoulos, S. Kombogiannis, J. Anastopoulos, and K. Efstathiou. Properties and performance of high aluminum containing (Ti,Al)N based supernitride coatings in innovative cutting applications. *Surface and Coatings Technology*, 177-178(0):727 – 734, 2004.

[7] R.F. Zhang and S. Veprek. Metastable phases and spinodal decomposition in $Ti_{1-x}Al_xN$ system studied by ab initio and thermodynamic modeling, a comparison with the TiN-Si_3N_4 system. *Materials Science and Engineering: A*, 448(1-2):111 – 119, 2007.

[8] I. Endler, M. Haehn, M. Herrmann, R. Pitonak, S. Ruppi, M. Schneider, H. van den Berg, and H. Westphal. Novel aluminum-rich $Ti_{1-x}Al_xN$ coatings by LPCVD. *Surface and Coatings Technology*, 203(5):530 – 533, 2008.

[9] J.M. Howe and B. Fultz. *Transmission Electron Microscopy and Diffractometry of Materials*. Springer, 2nd edition, 2002.

[10] L. Reimer and G. Pfefferkorn. *Raster-Elektronenmikroskopie*. Springer, 1973.

[11] L.A. Giannuzzi and F.A. Stevie, editors. *Introduction to Focused Ion Beams*. Springer, 2005.

[12] J. Keckes, M. Bartosik, R. Daniel, C. Mitterer, G. Maier, W. Ecker, J. Vila-Comamala, C. David, S. Schoeder, and M. Burghammer. X-ray nanodiffraction reveals strain and microstructure evolution in nanocrystalline thin films. *Scripta Materialia*, 67(9):748 – 751, 2012.

[13] C. Krywka, J. Keckes, S. Storm, A. Buffet, S. V. Roth, R. Döhrmann, and M. Müller. Nanodiffraction at MINAXS (P03) beamline of PETRA III. *Journal of Physics: Conference Series*, 425(7):072021, 2013.

[14] C. Riekel, M. Burghammer, and R. Davies. Progress in micro- and nano-diffraction at the ESRF ID13 beamline. *IOP Conference Series: Materials Science and Engineering*, 14(1):012013, 2010.

[15] L.B. Freund and S. Suresh. *Thin Film Materials: Stress, Defect Formation and Surface Evolution*. Cambridge University Press, 1st pbk. ed. edition, 2009.

[16] L. Spieß, R. Schwarzer, H. Behnken, and G. Teichert. *Moderne Röntgenbeugung*. Teubner Verlag, 1st edition, 2005.

[17] I.C. Noyan and J.B. Cohen. *Residual Stress: Measurement by Diffraction and Interpretation*. Springer, 1987.

[18] H. Yumoto, H. Mimura, S. Matsuyama, H. Hara, K. Yamamura, Y. Sano, K. Ueno, K. Endo, Y. Mori, M. Yabashi, Y. Nishino, K. Tamasaku, T. Ishikawa, and K. Yamauchi. Fabrication of elliptically figured mirror for focusing hard x rays to size less than 50 nm. *Review of Scientific Instruments*, 76(6):063708, 2005.

[19] G.E. Ice. Microbeam-Forming Methods for Synchrotron Radiation. *X-Ray Spectrometry*, 26(6):315–326, 1997.

[20] P. Kirkpatrick and A. V. Baez. Formation of Optical Images by X-Rays. *J. Opt. Soc. Am.*, 38(9):766–773, 1948.

[21] B. B. He. Introduction to Two-Dimensional X-ray Diffraction. *Powder Diffraction*, 18:71–85, 2003.

[22] W.C. Oliver and G.M. Pharr. Improved technique for determining hardness and elastic modulus using load and displacement sensing indentation experiments. *Journal of Materials Research*, 7(6):1564–1580, 1992.

[23] Liwei Shi, Yifeng Duan, Xianqing Yang, Gang Tang, Lixia Qin, and Liang Qiu. Structural, electronic and elastic properties of wurtzite-structured $Ti_xAl_{1-x}N$ alloys from first principles. *Materials Science in Semiconductor Processing*, 15(15):499–504, 2012.

[24] F. Tasnadi, I. A. Abrikosov, L. Rogstrom, J. Almer, M. P. Johansson, and M. Oden. Significant elastic anisotropy in $Ti_{1-x}Al_xN$ alloys. *Applied Physics Letters*, 97(23):231902, 2010.

[25] R. Ahuja, O. Eriksson, J. M. Wills, and B. Johansson. Structural, elastic, and high-pressure properties of cubic TiC, TiN, and TiO. *Phys. Rev. B*, 53:3072–3079, Feb 1996.

[26] Te-Hua Fang, Sheng-Rui Jian, and Der-San Chuu. Nanomechanical properties of TiC, TiN and TiCN thin films using scanning probe microscopy and nanoindentation . *Applied Surface Science*, 228(1-4):365 – 372, 2004.

[27] J. O. Kim, J. D. Achenbach, P. B. Mirkarimi, M. Shinn, and S. A. Barnett. Elastic constants of single-crystal transition-metal nitride films measured by line-focus acoustic microscopy. *Journal of Applied Physics*, 72(5):1805–1811, 1992.

[28] http://www.icdd.com/products/pdf2.htm. *International Centre for Diffraction Data*, September 2013.

[29] M. Wittmer, J. Noser, and H. Melchior. Oxidation kinetics of TiN thin films. *Journal of Applied Physics*, 52(11):6659–6664, 1981.

[30] A. Cavaleiro and J. Th. M. De Hosse, editors. *Nanostructured Coatings*. Nanostructure Science and Technology. Springer, 2006.

[31] P.H. Mayrhofer, A. Horling, L. Karlsson, J. Sjolen, T. Larsson, C. Mitterer, and L. Hultman. Self-organized nanostructures in the Ti-Al-N system. *Applied Physics Letters*, 83(10):2049–2051, 2003.